INTERNATIONAL JOURNAL FOR NUMERICAL METHODS IN FLUIDS
Int. J. Numer. Meth. Fluids 2012; **68**:1574–1604

A perturbation approach to large eddy simulation of wave-induced bottom boundary layer flows

Jeffrey C. Harris*,† and Stéphan T. Grilli

Department of Ocean Engineering, University of Rhode Island, Narragansett, RI 02882, U.S.A.

SUMMARY

We present the development, validation, and application of a numerical model for the simulation of bottom boundary layer (BL) flows induced by arbitrary finite amplitude waves. Our approach is based on coupling a 'near-field' local Navier–Stokes (NS) model with a 'far-field' inviscid flow model, which simulates large scale incident wave propagation and transformations over a complex ocean bottom, to the near-field, by solving the Euler equations, in a fully nonlinear potential flow boundary element formalism. The inviscid velocity provided by this model is applied through a (one-way) coupling to a NS solver with large eddy simulation (LES), to simulate near-field, wave-induced, turbulent bottom BL flows (using an approximate wall boundary condition by assuming the existence of a log-sublayer). Although a three-dimensional (3D) version of the model exists, applications of the wave model in the present context have been limited to two-dimensional (2D) incident wave fields (i.e. long-crested swells), while the LES of near-field wave-induced turbulent flows is fully 3D. Good agreement is obtained between the coupled model results and analytic solutions for both laminar oscillatory BL flow and the steady streaming velocities caused by a wave-induced BL, even when using open boundary conditions in the NS model. The coupled model is then used to simulate wave-induced BL flows under fully nonlinear swells, shoaling over a sloping bottom, close to the breaking point. Finally, good to reasonable agreement is obtained with results of well-controlled laboratory experiments for rough turbulent oscillatory BLs, for both mean and second-order turbulent statistics. Copyright © 2011 John Wiley & Sons, Ltd.

Received 13 September 2010; Accepted 23 January 2011

KEY WORDS: Navier–Stokes; marine hydrodynamics; boundary element methods; finite-volume methods; potential flow; turbulent flow; shallow water; nonlinear dynamics; validation

1. INTRODUCTION

Complex turbulent flows can be accurately modeled by solving Navier–Stokes (NS) equations, either by directly resolving all scales of turbulent motion (DNS, e.g. [1]) or in a time- or space-averaged sense, in combination with a turbulence closure scheme (e.g. [2]). Many methods and algorithms have been proposed for doing so (which have been detailed elsewhere). Here, we present the integration and application of a previously proposed large eddy simulation (LES, [3]) as a component of a new hybrid modeling approach for simulating wave-induced boundary layer (BL) flows. While more amenable to large size and high Reynolds number computations than DNS, the LES of complex three-dimensional (3D) flows over large and/or finely discretized domains still represents quite a formidable problem, despite the continual increase in computer performance. Hence, one must always try and limit the computational domain size to that necessary and sufficient for solving a given problem or physics, or even dimensionality (e.g. two-dimensional,

---

*Correspondence to: Jeffrey C. Harris, Department of Ocean Engineering, University of Rhode Island, Narragansett, RI 02882, U.S.A.
†E-mail: jcharris@oce.uri.edu

2D, versus 3D). For coastal wave dynamics problems, which typically extend over multiple spatial and temporal scales (e.g. from deep water to the shoaling and surf zones), it is often sufficiently accurate to use a simpler approach for a large part of the domain, to propagate and transform waves to the region of specific interest, in which 3D-NS simulations can then be more realistically performed. Using a 3D-NS solver for the entire domain would not only be computationally prohibitive, but would likely yield less accurate results (due to under-discretization and excessive numerical diffusion), than for instance much less costly inviscid flow solvers (even fully nonlinear, e.g. [4–6]) or higher order Boussinesq equation models (e.g. FUNWAVE [7, 8]). Furthermore, for long-crested swell, nearshore wave transformations can often be assumed to be 2D.

This has provided a rationale for the development of hybrid modeling approaches, in which different types of models are coupled and used in various regions of the fluid domain, where they are both more efficient and adapted to the dominant physics and scales in each given region (see, e.g. [9] for a review). Such models have already been applied to surfzone dynamics problems (e.g. [10–12]), wave structure interaction problems (e.g. [13]), and to model wave-induced flows and resulting sediment suspension over objects on the seabed (e.g. [14]). In the latter work, a so-called numerical wavetank (NWT) solving fully nonlinear potential flow (FNPF) equations was coupled to a 3D-LES in a somewhat heuristic manner.

As indicated above, the LES method used here is based on the approach of Zang *et al.* [3], who initially developed the NS solver and one of the subgrid scale (SGS) turbulence models being used here (dynamic mixed model, DMM) to study coastal upwellings [15, 16], and later modified the latter to study turbulent lid-driven cavity flows [3]; further modifications were done to study breaking interfacial waves [17] and suspended sediment transport [18, 19]. As discussed above, Gilbert *et al.* [14] coupled Zang *et al.*'s model to a 2D-NWT, to study wave-induced BL flows and sediment transport, through the addition to the NS model equations of the dynamic pressure gradient (equivalent to a body force) caused by waves, computed in the NWT. With this model, they were able to realistically (albeit quite qualitatively) simulate the suspended sediment transport over a partly buried circular obstacle, for a few periodic wave cycles. This implementation did not move beyond such simple cases, both because of the imperfect coupling between the LES and FNPF model equations and severe limitations of the LES grid size (as the code was not designed to take advantage of recent advances in distributed memory computing clusters).

We report here on more recent developments (in formalism, accuracy, and efficiency) of the techniques used in Gilbert *et al.* [14]. Specifically, in a new proposed hybrid approach, a modified and extended version of Zang *et al.*'s [3] 3D-NS-LES model is used in a perturbation scheme to simulate near-field, fine scale, turbulent bottom BL flows induced by arbitrary finite amplitude waves (i.e. 2D swells), whose propagation and nearshore transformation over larger scale bottom features, are modeled from the far- to the near-field in an inviscid flow model (i.e. NWT), which solves Euler equations in a FNPF formalism. The perturbation scheme consists in first dividing the total pressure and velocity fields into inviscid and viscous perturbation parts and then to rewrite NS equations for the perturbation fields only; this yields new forcing terms, which are function of inviscid flow fields representing incident wave forcing (e.g. similar to Kim *et al.* [20] and Alessandrini [21]). Moreover, in this approach, the computational domains for both NS-LES and FNPF models fully overlap, which makes it easy passing information from one domain to the other, although here we will just illustrate a one-way coupling, from large to fine scales flows. Additionally, this coupling method is very relevant to the physics of wave-induced flow problems since, for non-breaking waves and outside of BLs, the bulk of the flow is nearly inviscid.

It should be noted that developments of Zang's LES also continued independently to those presented here in relation to the hybrid coupled modeling approach. Thus, Cui and Street [22] implemented a parallelized version of the code, which allowed for much larger computational domains. Grilli *et al.* [23] used this latter version to begin testing its suitability for wave-induced BLs, with the goal of again coupling it to an FNPF-NWT. A completely separate development of Cui and Street's code for bedform evolution was done by Chou and Fringer [24, 25]. Other, unrelated research groups, have also been actively studying the application of LES to turbulent oscillatory BLs (e.g. [26, 27]). While the LES, SGS models, and perturbation method presented here have all been used in one form or another by previous researchers, the particular integration of these three components into an accurate and efficient parallelized implementation, well suited to coastal engineering problems, is new and unique. Additionally, the coupling to a 2D-FNPF-NWT, and potentially in future developments to a similar 3D-NWT (e.g. [28]) makes it possible to use a variety of fully realistic nonlinear and irregular wave forcings, besides the commonly used simple oscillatory or linear wave flows (see e.g. [29]).

In summary, in this paper, we present recent improvements and validation of a new hybrid method applied to simulating oscillatory and wave-induced BL flows with a 3D-LES. For validation we compare simulation results to analytic solutions of laminar flows and to experimental results of rough turbulent oscillatory BLs. In our hybrid/perturbation approach, the total velocity and pressure fields are expressed as the sum of irrotational (thus kinematically inviscid) and near-field viscous perturbations above a rigid seafloor. The NS equations are formulated and solved for the perturbation fields only, which are forced by additional terms representing the incident fields. In the present applications, these are given either analytically or numerically obtained in a coupled 2D-FNPF-NWT.

2. OSCILLATORY BL FLOW PHYSICS AND MODELS

A wide range of approaches besides LES has been proposed for modeling turbulent oscillatory BLs, often in the context of wave-induced flow on the seafloor. The earliest approaches were merely empirical relationships or were based on a time-varying logarithmic BL assumption. Kajiura [30] considered a piecewise varying eddy viscosity distribution. Grant and Madsen [31] used a mixing-length approach where eddy viscosity was proportional to the height above the bed. These and other similar works all reported good agreement with mean flow measurements, but did not model turbulent statistics well if at all. Only later models, like Trowbridge and Madsen's [32] or Davies's [33], considered a time-varying eddy viscosity, which is experimentally observed. More recently, Reynolds-averaged NS models (RANS) of turbulent oscillatory BLs have been used extensively which provided reasonable to good agreement with experiment for both mean flow and second-order turbulent statistics (e.g. [34–40]). In those, many different turbulence models were used, from Saffman's energy-vorticity turbulence model, used by Blondeaux, to a high Reynolds number $k-\varepsilon$ model used by Justesen, or the two-equation turbulence closure of Chien, used by Thais *et al.*

The flow in a purely oscillatory BL over a solid horizontal wall is driven by a periodic pressure gradient. In the simplest case the forcing flow is represented by a sinusoidal free-stream (inviscid) velocity given by $u_i^I = \delta_{i1} U_0 \sin \omega t$, where U_0 is the amplitude and ω the angular frequency. Far away from the wall, water particles follow the free-stream and oscillate with an amplitude on the order $A = U_0/\omega$. In the BL, the flow additionally depends on the kinematic viscosity, ν and, for rough boundaries, on the Nikuradse roughness length, k_s. The BL flow regime is thus dependent on two non-dimensional numbers: (i) a relative roughness, A/k_s and (ii) the Reynolds number, $U_0 A/\nu$. Figure 1 shows various regime regions identified based on values of those two parameters. Various authors (e.g. [34, 41, 45]) have proposed slightly different or additional regions, but in general the flow regime can either be described as laminar, smooth turbulent, rough turbulent, or transitional. To a first order, wave-induced oscillatory BLs can be characterized in the same way. In this paper, we will consider both laminar and rough turbulent conditions.

Many measurements of turbulent oscillatory BLs have been reported, usually made in an oscillatory water tunnel (e.g. [44]), or a reciprocating wind tunnel (e.g. [46]), resulting in many advances in understanding oscillatory BLs. Measurements from wavetanks (e.g. [42]) are possible, but except in the largest wavetanks it is not usually possible to reproduce the high Reynolds number flows that are present in the ocean. Thus, Jonsson and Carlsen [44] measured mean flow velocities over rough walls in an oscillatory water tunnel for two different rough turbulent tests. They found that the velocity at points just above the rough bed could be well described by a log-layer

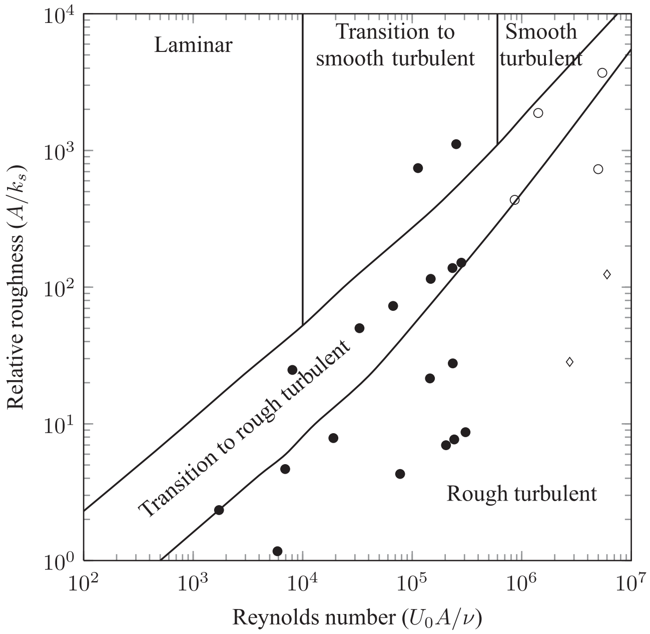

Figure 1. Oscillatory BL flow regimes as a function of Reynolds number and relative roughness, as estimated by Kamphuis [41] and overview of conditions observed in selected experiments (●—Sleath [42]; ○—Jensen *et al.* [43]; and ◇—Jonsson and Carlsen [44]).

assumption. Hino *et al.* [46] measured mean flow velocities, turbulent intensities, Reynolds stresses and turbulent-energy production rates for oscillatory BLs over a smooth wall. Interestingly, they found that the spectral decay of the turbulent energy in the decelerating phase is steeper than the 5/3 power law of the Kolmogorov spectrum (see e.g. Pope [47] for a general description of spectral analysis of turbulence). Sleath [48] was one of the first to measure both turbulent intensity and mean flow velocity for oscillatory BLs over rough surfaces. Notably Sleath found that the time-averaged eddy viscosity near the rough bed was negative, meaning that the turbulent momentum is transported against the mean velocity gradient, which implies that the turbulent kinetic energy production is negative. Sleath suggested that this was due to jets of fluid moving away from the wall near flow-reversals. Jensen *et al.* [43] measured mean flow velocity and turbulent intensity over both smooth and rough walls.

Although far from the boundary wave-induced BLs tend toward an inviscid solution, wave-induced BLs differ from purely uniform oscillatory BLs in that weak vorticity is present at moderate distances from the seabed. While to a first order this is typically insignificant, it does induce a steady streaming velocity. Longuet-Higgins derived a theory describing steady streaming velocity profiles for wave-induced laminar BL flows [49] or with time-invariant eddy viscosity distributions [50]. Trowbridge and Madsen [32] developed a model which instead considered a time-varying eddy viscosity distribution. Since then, Reynolds-averaged approaches have been commonly used for representing wave-induced BLs (e.g. [51–55]). A more practical model of drift over very rough beds was developed by Davies and Villaret [56] where the dominant process is vortex shedding as opposed to random turbulence. Recently, Myrhaug and Holmedal [57] derived the steady streaming induced by random waves, in both laminar and turbulent conditions. Others have focused on the effects of wave asymmetry. Scandura [58] numerically modeled steady streaming for a transitionally turbulent BL forced by a pressure gradient with two harmonics. Holmedal and Myrhaug [59] have considered the combination of Longuet-Higgins steady streaming and wave asymmetry, as well as their relative contributions to the overall steady streaming velocities for different parameters and for both sinusoidal and Stokes second-order waves. Note, in the present approach, the coupling of the 3D-LES to the fully nonlinear NWT, which also allows representing arbitrary bottom bathymetry, makes it possible to simulate the wave-induced forcing flow from fully realistic, strongly nonlinear (near-breaking), shoaling waves, which are both trough-crest and front-rear asymmetric.

When deriving a theory for wave-induced steady streaming over constant depth in a very thin BL (as compared with the wavelength), only the horizontal component of the inviscid forcing needs to be considered [60]. In this context, earlier theoretical and numerical research has focused on sinusoidal or second-order Stokes waves. Under sinusoidal waves, the steady streaming velocity is always in the direction of wave propagation [49], whereas under second-order Stokes waves, streaming is reduced or may be in the opposite direction [59]. Higher order wave forcing of course provides more realistic conditions, which, as indicated above, can be obtained from simulations in an FNPF-NWT, such as Grilli and Subramanya's [4] 2D-NWT. In the latter, as in many similar NWTs, continuity is satisfied by solving Laplace's equation for the velocity potential with a boundary element method (BEM), and the nonlinear kinematic and dynamic free surface boundary conditions are integrated in time with a mixed Eulerian–Lagrangian (MEL) scheme. The MEL scheme was first introduced in this context by Longuet-Higgins and Cokelet [61] and allowed for simulating overturning waves. (A similar 3D-NWT was developed by Grilli *et al.* [28].) In this work, we compare the effects of a variety of forcing functions on the oscillatory BL flow.

While Longuet-Higgins [49] validated his theory using earlier measurements, Russell and Osorio [62] and Collins [63] further confirmed that the drift velocity at the edge of the BL matched Longuet-Higgin's theory for laminar flows over a flat bed. Because this velocity was independent of viscosity, Longuet-Higgins [50] suggested that, for a constant eddy viscosity, the same result would hold in turbulent conditions. Johns [64] extended this argument to vertically varying but time-independent eddy viscosity models, typical of the time. Collins' [63] measurements suggested that this was not true at higher Reynolds numbers, which has since been confirmed by Brebner *et al.* [65], Bijker *et al.* [66], and van Doorn [67]. More recent studies have focused on other effects in the BL. The effect of wave asymmetry acts opposite to the effect of Longuet-Higgins steady streaming, as has been studied by Ribberink and Al-Salem [68] in an oscillating water tunnel. Many studies are focused on either flat seabeds or naturally occurring bedforms. Marin [69] studied Eulerian drift for progressive waves over a rippled bed in the transitionally turbulent regime, and found that the Davies and Villaret [56] model for turbulent flow could be adjusted to handle transitionally turbulent conditions.

3. GOVERNING EQUATIONS

NS equations for an incompressible, isothermal, Newtonian fluid read as:

$$\frac{\partial u_i}{\partial x_i} = 0 \tag{1}$$

$$\frac{\partial u_i}{\partial t} + \frac{\partial}{\partial x_j}\left(u_i u_j + \frac{p}{\rho}\delta_{ij} - \nu \frac{\partial u_i}{\partial x_j}\right) = 0 \tag{2}$$

where u_i and p are the water velocity and dynamic pressure, respectively, in a fluid of density ρ and kinematic viscosity ν. We adopt the indicial tensor notation convention, with x_3 denoting a vertical distance measured from some reference point.

Let us denote by (u_i^I, p_I) the velocity and pressure fields of the ocean wave flow, considered to be inviscid outside of thin BLs. Such flows are well described by Euler equations:

$$\frac{\partial u_i^I}{\partial x_i} = 0 \tag{3}$$

$$\frac{\partial u_i^I}{\partial t} + \frac{\partial}{\partial x_j}\left(u_i^I u_j^I + \frac{p_I}{\rho}\delta_{ij}\right) = 0 \tag{4}$$

DOI: 10.1002/fld

Let us then introduce a decomposition of the total viscous flow into the sum of the latter inviscid free-stream flow and a defect or perturbation flow, of velocity u_i^P and pressure p_P:

$$u_i = u_i^I + u_i^P \tag{5}$$

$$p = p_I + p_P \tag{6}$$

Replacing Equations (5) and (6) into Equations (1) and (2), and subtracting Equations (3) and (4), we derive the governing equations for the perturbation fields as:

$$\frac{\partial u_i^P}{\partial x_i} = 0 \tag{7}$$

$$\frac{\partial u_i^P}{\partial t} + \frac{\partial}{\partial x_j}\left(u_i u_j - u_i^I u_j^I + \frac{p_P}{\rho}\delta_{ij} - \nu\frac{\partial u_i}{\partial x_j}\right) = 0 \tag{8}$$

Here, the perturbation is defined in a region encompassing the near-field bottom BL of interest.

Although formally different, for the range of problems studied here, these equations can be shown to be equivalent to the forcing of the total flow with the inviscid wave dynamic pressure gradient proposed by Gilbert *et al.* [14], expressed as:

$$\frac{\partial u_i}{\partial x_i} = 0 \tag{9}$$

$$\frac{\partial u_i}{\partial t} + \frac{\partial}{\partial x_j}\left(u_i u_j + \frac{p_P}{\rho}\delta_{ij} - \nu\frac{\partial u_i}{\partial x_j}\right) = -\frac{1}{\rho}\frac{\partial p_I}{\partial x_j} \tag{10}$$

There are two key advantages, however, to the current approach, as compared with this earlier work: (1) boundary conditions can be more clearly and accurately defined for the viscous perturbation (i.e. as vanishing or using a radiation condition away from the wall); and (2) only the inviscid velocity is needed in the NS forcing terms rather than the dynamic pressure gradient.

By applying a spatial-average operator (overbar) to the NS equations we obtain the momentum equation for the resolved perturbation as

$$\frac{\partial \bar{u}_i^P}{\partial x_i} = 0 \tag{11}$$

$$\frac{\partial \bar{u}_i^P}{\partial t} + \frac{\partial}{\partial x_j}\left(\bar{u}_i \bar{u}_j - \overline{u_i^I u_j^I} + \frac{\overline{p_P}}{\rho}\delta_{ij} - \nu\frac{\partial \bar{u}_i}{\partial x_j} + \tau_{ij}\right) = 0 \tag{12}$$

where τ_{ij} is the SGS stress defined as:

$$\tau_{ij} = \overline{u_i u_j} - \bar{u}_i \bar{u}_j \tag{13}$$

Note that, typically, SGS models only consider the deviatoric stress $\tau_{ij} - \tau_{kk}/3$, because the resolved turbulent pressure, $\bar{p}^*$, is different from the resolved hydrodynamic pressure with:

$$\frac{\bar{p}^*}{\rho} = \frac{\bar{p}}{\rho} + \frac{1}{3}\tau_{kk} \tag{14}$$

For the SGS models considered here, we define

$$\tau_{ij} - \frac{\delta_{ij}}{3}\tau_{kk} = -2\nu_T \bar{S}_{ij} + C_r\left(L_{ij}^m - \frac{\delta_{ij}}{3}L_{kk}^m\right) \tag{15}$$

where ν_T is the eddy viscosity, $\bar{S}_{ij}$ is the resolved shear strain rate, L_{ij}^m is the modified Leonard term, and C_r is a constant coefficient (either one or zero, depending on the SGS decomposition used).

DOI: 10.1002/fld

3.1. Discretization

The governing equations are discretized in 3D as in Cui and Street [22], i.e. using a finite-volume formulation with second-order accuracy in both time and space on a non-staggered grid. Quadratic upstream interpolation for convective kinematics (QUICK) [70] is used to discretize the convective terms of the fluid flow, and second-order centered differences are used for the remaining terms. The convective terms are time integrated using the second-order Adams–Bashforth technique, and the diffusive terms with a second-order implicit Crank–Nicolson scheme. The Poisson equation for the pressure field is solved with a multigrid technique. Note that in our hybrid approach, the inviscid velocity field is obtained directly from another model—in this paper, a theoretical solution or a 2D-NWT—and is not subject to the numerical errors of the NS solver.

For all the test cases that are considered here, the computational domain is a box, L_1 long in the streamwise direction, L_2 wide in the spanwise direction, and L_3 high in the vertical direction. The corresponding number of gridpoints are N_1, N_2, and N_3, respectively.

For post-processing, it is useful to define variables in terms of integrals that, when discretized are sums, e.g. ensemble averages. Thus, for an arbitrary variable q that is aperiodic, the average over a horizontal plane is:

$$\langle q\rangle(x_3)=\frac{1}{L_1L_2}\int\int q\,\mathrm{d}x_1\,\mathrm{d}x_3 \tag{16}$$

calculated as,

$$\langle q\rangle([x_3]_j)=\frac{1}{N_1N_2}\sum_i\sum_k[q]_{i,j,k} \tag{17}$$

where here the additional subscripts $[]_{i,j,k}$ are grid indices (with e.g. i varying from 1 to N_1), whereas for periodic field variables, an ensemble average can be made more accurate by also averaging over several periods (e.g. $\langle q\rangle(x_3)=(1/N)(1/L_1L_2)\sum_{n=1}^{N}\int_0^{L_1}\int_0^{L_2}q(x_1,x_2,x_3,t+nT/2)$ $\mathrm{d}x_1\,\mathrm{d}x_2$ or $\langle q\rangle(x_3)=(1/N)(1/L_1L_2)\sum_{n=1}^{N}(-1)^n\int_0^{L_1}\int_0^{L_2}q(x_1,x_2,x_3,t+nT/2)\,\mathrm{d}x_1\,\mathrm{d}x_2$ depending on whether the field variable is periodic or antiperiodic, such as the turbulent intensity or the mean velocity, respectively).

In theoretical models, oscillatory BLs are often considered to be ‘infinitely long’, which would correspond to a half-plane or half-space. This may represent physical circumstances quite well but is not practical in a numerical model where we want to limit the domain size to limit computational requirements. Hence, assuming the flow is statistically homogenous in a direction, we can apply periodic boundary conditions, with the premise that velocity fluctuations a half-domain away are completely uncorrelated with one another. Such space-periodicity conditions will be used for some of the applications presented here.

While the numerical method is designed to handle any structured 3D grid, here we limit our consideration to two types—regular grids in each direction and regular grids with exponential stretching in the vertical direction. The latter is based on a stretching ratio based on the vertical distance between adjacent gridpoints (e.g. a 1.1-stretching ratio would correspond to a 10% increase in cell size with each step in the vertical direction).

Note that this vertical stretching induces a large aspect ratio for the cells near the boundary. Consider a grid with a seabed of height $h(x_1,x_2)$, and vertical grid spacing Δx_3. From a vertical profile it may appear that eddies of $O(\Delta x_3)$ are resolved, for example an aspect ratio of 10:1 the grid filter acts on a volume of approximately $O(10^2\Delta x_3^3)$, though near-wall eddies are expected to be $O(2\kappa(x_3-h))$ across, so turbulent eddies near the surface are not resolved (e.g. when $2\kappa 10^{-2/3}\gtrsim\Delta x_3/(x_3-h)$). These estimates are most accurate for flat seabeds, but analogous arguments can be made for complex bathymetry. Thus we expect an underprediction of turbulent intensity near the wall, and a need to augment the SGS stresses. The method used is described in the following section.

3.2. Bottom boundary condition

In all cases considered here, the bottom boundary condition is a no-flux condition with a shear stress applied depending on flow conditions, i.e.

$$\tau_w = \rho \nu \left[\frac{\partial \bar{u}_{\tan}}{\partial n} \right]_{x_3 = h(x_1, x_2)} \tag{18}$$

where n is the normal direction to the wall, $\bar{u}_{\tan}$ is the resolved velocity tangential to the wall, and τ_w is the wall shear stress. In the BL theory, the latter is typically defined as a function of the friction velocity u_*, as: $\tau_w = \rho u_*^2$, which yields

$$\left[\frac{\partial \bar{u}}{\partial n} \right]_{x_3 = h(x_1, x_2)} = \frac{1}{\nu} u_*^2 \tag{19}$$

Combining this with the condition that the eddy viscosity is zero along the bed, the boundary condition can be implemented as a purely viscous wall stress. Numerically, this velocity gradient condition is implemented through using layers of additional (ghost) cells, located outside of the domain. We apply one of the two boundary friction velocity models, depending on the application. In each case we evaluate them for the gridpoints adjacent to the boundary (e.g. over a flat bed, at $x_3 = h(x_1, x_2) + \Delta x_3/2$). To be unambiguous for curved seabeds, we specify z_1 to be the distance of the center of the first grid cell to the boundary.

For laminar tests, we consider a no-slip condition such that:

$$u_* = \sqrt{\frac{\bar{u}_{\tan} \nu}{z_1}} \tag{20}$$

For rough turbulent cases, we assume that the von Karman–Prandtl equation (for a logarithmic sublayer) can be applied at the first gridpoint above the bed. For hydraulically rough conditions, this reads as:

$$\frac{\bar{u}_{\tan}}{u_*} = \frac{1}{\kappa} \log \frac{z_1}{z_0} \tag{21}$$

where κ is the von Karman constant, taken to be 0.41, and z_0 is the roughness length, which can be related to the Nikuradse roughness, $k_s = 30 z_0$. Such a log-layer equation is known to be applicable in only a narrow regime of flows of engineering interest, but it is a common practice to apply this in LES models of atmospheric flows [71]. For other approximate bottom boundary conditions see Cabot and Moin [72] and for a review of LES wall modeling see Piomelli and Balaras [73]. The use of the log-layer law is also supported by the experiments of Nakayama *et al.* [74]. Note that Nakayama *et al.*'s experiments considered a zero-pressure gradient, and did not include flow separation. These wall models may be unsuitable for situations with turbulent flow separation, but this is an issue to be considered in future work.

3.3. Subgrid scale models

Since no turbulence closure scheme has been found satisfactory for all situations, a variety of SGS models have been developed for LESs. Most models are some variants of the Smagorinsky model, where the SGS stress is an algebraic function of the resolved shear stress rate. In this work, we consider several models for comparison, including the Smagorinsky model, the dynamic Smagorinsky model (DSM), and DMM. Note that, as in Cui and Street [22], the spatial gradient of eddy viscosity is neglected in the discretized governing equations.

3.3.1. Smagorinsky model. The Smagorinsky model [75] of the SGS stress

$$\tau_{ij} - \frac{\delta_{ij}}{3} \tau_{kk} = -2 \nu_T \bar{S}_{ij} \tag{22}$$

DOI: 10.1002/fld

is an algebraic function of the resolved shear strain rate tensor

$$\bar{S}_{ij} = \frac{1}{2}\left(\frac{\partial \bar{u}_i}{\partial x_j} + \frac{\partial \bar{u}_j}{\partial x_i}\right) \tag{23}$$

where $|\bar{S}|$ is the magnitude of the shear strain rate tensor:

$$|\bar{S}| = \sqrt{2\bar{S}_{ij}\bar{S}_{ij}} \tag{24}$$

The eddy viscosity, ν_T, is expressed as proportional to the magnitude of the local shear strain rate as

$$\nu_T = C_s \bar{\Delta}^2 |\bar{S}| \tag{25}$$

where C_s is the Smagorinsky model coefficient (the square of the Smagorinsky constant) and $\overline{\Delta}$ is a grid-filter width that can be expressed from the Jacobian J of the coordinate transformation as: $\bar{\Delta} = J^{1/3}$, or, for a Cartesian grid, as: $\bar{\Delta} = (\Delta x_1 \Delta x_2 \Delta x_3)^{1/3}$. At a wall, the discretized shear strain rate tensor is calculated with one-sided finite differencing, since the shear imposed as a boundary condition is non-physical.

Lilly [76] found that for the Smagorinsky model to agree with the Kolmorgorov turbulence spectrum for isotropic turbulence, the Smagorinsky constant must be approximately 0.16. It is well known that this overpredicts the amount of dissipation for wall-bounded flows. Here, we use a Smagorinsky constant of 0.145 (i.e. model coefficient of 0.021), which is consistent with the earlier work of Gilbert *et al.* [14].

3.3.2. Dynamic Smagorinsky model. The next major advancement in SGS modeling was the DSM of Germano *et al.* [77], whereby the Smagorinsky coefficient in Equation (25) is allowed to vary in time and space. At each point, following a procedure of Lilly [78] and Germano [79], the coefficient C_s is assumed to be scale-invariant. As a result, Equations (22)–(25) can be defined for two different length scales (known as the filter widths), and then at each point the local C_s can be chosen to be that which minimizes the least-squares error in the above equations.

In order to obtain the velocity fields at the appropriate length scales, the resolved velocity field is used, as well as a filtered version of the velocity field. Often a simple discrete filter (e.g. using the trapezoidal rule) is used, and typically the grid size ratio α is chosen as 2.0, based on the analysis of Germano *et al.* [77] (i.e. smaller values gave less accurate results, whereas larger values provided no clear advantage). Lund [80] showed that often the filter width is not properly determined, so while we use the same test-filter as Cui and Street [22], we use Lund's more accurate filter-width definition of $\alpha \approx \sqrt{6} = 2.46$, see [80] for details.

While the DSM requires fewer input parameters than a simple Smagorinsky model, and is typically more accurate, this least-squares procedure for finding the model coefficient can lead to numerical instabilities. Here, as in Zang [15], C_s is local filtered, and a cutoff is implemented, preventing negative total viscosity (i.e. if the local eddy viscosity is calculated less than the kinematic molecular viscosity, it is set equal to $-\nu$).

3.3.3. Dynamic mixed model. Here, the SGS stresses are modeled using Zang *et al.*'s [3] DMM, based on the stress decomposition proposed by Germano [81]:

$$\tau_{ij} = L_{ij}^m + C_{ij}^m + R_{ij}^m \tag{26}$$

which consists in a sum of the modified Leonard term, modified cross term, and modified SGS Reynolds stress, defined as

$$L_{ij}^m = \overline{\bar{u}_i \bar{u}_j} - \bar{\bar{u}}_i \bar{\bar{u}}_j \tag{27}$$

$$C_{ij}^m = \overline{\bar{u}_i u'_j + u'_i \bar{u}_j} + \bar{\bar{u}}_i \overline{u'_j} - \overline{u'_i} \bar{\bar{u}}_j \tag{28}$$

$$R_{ij}^m = \overline{u'_i u'_j} - \overline{u'_i}\,\overline{u'_j}. \tag{29}$$

respectively. Then, by modeling the SGS stress as

$$\tau_{ij}-\frac{\delta_{ij}}{3}\tau_{kk}=-2C_s\bar{\Delta}^2|\bar{S}|\bar{S}_{ij}+L^m_{ij}-\frac{\delta_{ij}}{3}L^m_{kk} \tag{30}$$

and again assuming scale independence, the optimal model coefficient can similarly be found by applying Germano's technique.

3.3.4. Near-wall eddy viscosity. One of the premises of SGS models is that the spatial filtering involved is over regions of small flow variations. This is not true, however, near a boundary when using an approximate boundary condition such as Equation (21) (see e.g. Cabot and Moin [72]). Specifically, near a wall, the grid filter width is approximately x_3-h, but the largest eddies are only $\kappa(x_3-h)$) across. This affects the eddy viscosity in the near-wall region in a way which is model-specific. For the constant coefficient Smagorinsky model, for instance, it is well known that the near-wall eddy viscosity is overpredicted. Because this behavior and limitations of the Smagorinsky model have been well documented in the literature, we do not modify this model, to use it as a 'control' model in our work. The DSMs, by contrast, underpredict the near-wall eddy viscosity to the point that some modifications are necessary. The first change we make to the standard dynamic SGS models, to account for effects of the boundary, is to adjust the filtering operator (i.e. a box-filter of the resolved velocity). Filtering at points near the wall will result in a solution that depends on non-physical values at the ghost cells outside of the domain. Hence, near the boundary, we use instead the commutative filters of Vasilyev *et al.* [82] which are one-sided for points adjacent to a boundary. The resulting filtered velocity field is mathematically consistent throughout the domain, and depends only on points within the domain. Similarly, some care is taken to use one-sided finite differences in computing the shear strain rate at points near the boundary.

Additionally, following Chow and Street [83] and Chow *et al.* [84], the eddy viscosity at the wall in the SGS model is increased, in order to augment the near-wall shear stresses. Here, we follow Zedler and Street [19], who by specifying the eddy viscosity as

$$(\nu_T)_{\text{total}}=(\nu_T)_{\text{SGS}}+\kappa u_*(x_3-h)\cos^2\left(\frac{\pi(x_3-h)}{4\Delta x_1}\right) \tag{31}$$

for all points between the bed and a height $2\Delta x_1$. This can also be expressed as

$$(\nu_T)_{\text{total}}=(\nu_T)_{\text{SGS}}+\kappa u_* z\cos^2\left(\frac{\pi z}{4\sqrt{J/2z_1}}\right) \tag{32}$$

for $z<2\sqrt{J/2z}$, z is the distance from a point to the seabed, and as before, z_1 is the distance of the center of the first grid cell to the boundary, and J is the Jacobian of the transformation used in deriving the discretized governing equations.

This scheme increases the near-wall stress and smoothly varies the eddy viscosity from that in the inner wall modeled region to the outer region in the LES domain. Note, this technique has similarities with both RANS modeling (since the filter width is horizontally large and the eddy viscosity is given from a mixing length theory) and wall models, since the eddy viscosity is dependent upon a height above the bed, which is not well defined for general surfaces. Preliminary tests, which will be detailed below as part of the turbulent BL application, confirmed that when an augmented near-wall stress term such as Equation (32) is not included, results are qualitatively similar, but the wall stress is underpredicted by as much as 50%. See Piomelli *et al.* [85] and Chow *et al.* [84] for the recent advances in using even more sophisticated techniques for augmenting near-wall stresses in an LES.

3.4. Fully nonlinear potential flow

In this work, we use different unsteady inviscid flow solutions to force the LESs of the BL flow. Some are simple analytical solutions (such as a uniform oscillatory flow) but, to simulate realistic wave forcing, we use the results of a 2D-NWT based on the FNPF theory (i.e. in which fully nonlinear kinematic and dynamic free surface boundary conditions are kept in an MEL formalism [4–6]). Governing equations and numerical methods for this 2D-NWT are briefly summarized below, in the context of the perturbation approach introduced before.

For incompressible irrotational flows, we define $u_k^I = \partial\Phi/\partial x_k$, with Φ the velocity potential. With this definition, mass conservation becomes Laplace's equation

$$\nabla^2\Phi = 0 \tag{33}$$

which is efficiently and accurately solved using a higher order BEM based on Green's second identity

$$\alpha(x_j)\Phi(x_j) = \int_\Gamma \left\{ \frac{\partial\Phi(x_i)}{\partial n} G_{ij} - \Phi(x_i)\frac{\partial G_{ij}}{\partial n} \right\} \mathrm{d}\Gamma(x_i) \tag{34}$$

where $\Gamma(x_i)$ denotes the NWT boundary, n_i is the outwards unit normal vector to the boundary (Figure 2), G_{ij} is the free-space Green's function given in 2D by

$$G(x_i, x_j) = -\frac{1}{2\pi}\log|x_i - x_j| \tag{35}$$

where x_i and x_j are both points on the boundary, with the latter referred to as a collocation node, and α is a coefficient function of the angle of the boundary at x_j.

On the free surface Γ_f (Figure 2), the fully nonlinear kinematic and dynamic boundary conditions

$$\frac{\mathrm{D}r_i}{\mathrm{D}t} = \frac{\partial\Phi}{\partial x_i} \tag{36}$$

$$\frac{\mathrm{D}\Phi}{\mathrm{D}t} = -gx_3 + \frac{1}{2}\frac{\partial\Phi}{\partial x_i}\frac{\partial\Phi}{\partial x_i} - \frac{p_a}{\rho} \tag{37}$$

respectively (where x_3 is the vertical coordinate), are time integrated using second-order Lagrangian Taylor series expansions, for the free surface position r_i and potential $\Phi(r_i)$ (i.e. using both Φ and $\partial\Phi/\partial t$, and their normal and tangential derivatives), and an explicit time stepping scheme. A (Neumann) no-flow or specified normal velocity condition is specified on the other NWT boundaries, including a wavemaker and the seabed.

The above boundary integral equations are discretized, as detailed in Grilli and Subramanya [4], for a series of collocation nodes x_j, $j = 1, \ldots, N_\Gamma$ on the boundary, and using higher order elements to interpolate between the nodes. The resulting linear system of equations is solved at each time step to provide boundary values of Φ and its normal and time derivatives, which in turn are used in the time updating of free surface solution.

Wave generation in the NWT can be accomplished in several ways. For the application presented here, generation using a flap wavemaker is simulated at the leftward boundary of the NWT, Γ_w, by specifying a (horizontal) stroke motion, $x_w(t)$, similar to that of a physical wavetank (Figure 2).

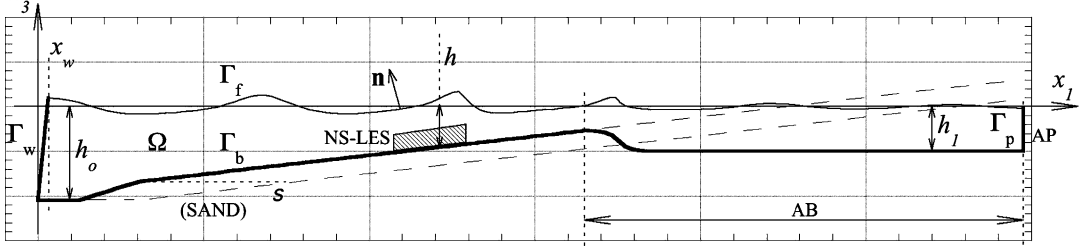

Figure 2. Sketch of the 2D-NWT setup for computations of wave shoaling over a slope. Note that AB is absorbing beach for $x \geqslant x_a$; here a flap wavemaker is located at $x = x_w$, but other wave generation methods are possible.

DOI: 10.1002/fld

With this method, regular waves can be easily generated (e.g. [5, 6]), as well as more complex wave climates.

In the far-field wave domain, incident waves propagate, transform, and shoal over the specified sloping bottom topography, as simulated in the NWT. In the near-field, waves would eventually overturn and break, and dissipate their energy. To prevent breaking in the NWT, which would interrupt FNPF computations, following Grilli and Horrillo [5], incident wave energy is gradually dissipated in an absorbing beach (AB) at the far shallower end of the NWT and using an actively absorbing lateral piston (AP) boundary (Figure 2). In the AB, energy dissipation results from the (negative) work against waves of an absorbing surface pressure p_{a}, specified in the dynamic free surface boundary condition, proportional to the normal particle velocity as

$$p_a(x_1,t)=v_a(x_1)\frac{\partial\Phi}{\partial n} \tag{38}$$

where v_a denotes a smoothly varying AB absorption function in the long NWT horizontal direction x_1 (see [5] for detail).

The NS model grid is finely discretized and thus may have millions of gridpoints; hence it could be computationally expensive to calculate the BIE solution in the NWT for every such internal point. For turbulent cases considered by Gilbert *et al.* [14], assuming fairly long and regular incident waves, this was tackled by computing the inviscid wave velocities only at a subset of the NS gridpoints and then interpolating over the entire NS grid. Internal velocities were computed in the NWT using a boundary integral equation (note this is also a mathematically exact equation):

$$u_k(x_j)=\int_\Gamma\left\{\frac{\partial\Phi(x_i)}{\partial n}(\nabla_k G_{ij})-\Phi(x_i)\left(\nabla_k\frac{\partial G_{ij}}{\partial n}\right)\right\}\,\mathrm{d}\Gamma(x_i) \tag{39}$$

Because the present applications of the coupled NWT-NS-LES are only for wave-induced flows within a very thin BL, the vertical variation of the inviscid velocity can be neglected within the BL. Accordingly, the inviscid forcing velocity in the BL is computed for a series of grid cell horizontal abscissa x_{g1} at seabed points, as

$$u_1^I(x_{g1},t)\approx\left(\frac{\partial\Phi}{\partial x_1}\right)_{(x_{g1},h(x_{g1}))} \tag{40}$$

$$u_2^I(x_{g1},t)=0.d0 \tag{41}$$

$$u_3^I(x_{g1},t)\approx\left(\frac{\partial\Phi}{\partial x_3}\right)_{(x_{g1},h(x_{g1}))} \tag{42}$$

This assumption is reasonable because for the application on a sloping bed shown below, the bed slope m is very small, and because the simulation domain is very thin. This approximation is further justified below in the presented application, where it is used when the incident wavelength is very large with respect to the BL thickness. These internal velocities are then used to force the NS-LES model, as detailed above.

4. APPLICATIONS

4.1. Laminar wave-induced boundary layers

4.1.1. Stokes boundary layer. Stokes' second problem [86] provides an exact solution for the horizontal velocity profile in a laminar BL of thickness $\delta_{\mathrm{S}}=\sqrt{2\nu/\omega}$ (known as the Stokes-layer thickness), forced by an oscillatory flow of angular frequency $\omega=2\pi/T$ or period T. A major feature of laminar oscillatory BLs is that the phase lag between the wall shear stress, τ_w, and the

DOI: 10.1002/fld

free-stream velocity is 45°. For other regimes, however, this angle varies. In the following test case, the inviscid flow forcing is simply a spatially uniform horizontal, sinusoidal flow:

$$u_i^I = \delta_{i1} U_0 \sin \omega t \tag{43}$$

where U_0 is the amplitude of the free-stream velocity. The analytical solution of Stokes' second problem yields the following horizontal velocity:

$$u_{a1} = U_0(1 - \exp[-(x_3 - h)/\delta_S]) \sin(\omega t - (x_3 - h)/\delta_S) \tag{44}$$

Figure 3 shows the vertical profiles of horizontal velocity at a few phases of the flow, based on this solution.

As a numerical a first validation test of the implementation of the perturbation approach in the NS model, we computed such laminar oscillatory BL flows for a variety of grid sizes and time steps, setting the Reynolds number based on Stokes-layer thickness to: $Re_\delta = U_0 \delta_S / \nu = 1$ (note, here, of course, the LES is not called upon and the eddy viscosity is set to zero). Spatial periodicity was assumed in the horizontal direction and a no-slip boundary condition was specified on the bed. The grid is 16 Stokes thicknesses high, and 1 Stokes thickness wide in both horizontal directions. For each test case, four points in each horizontal directions are used (though for a 2D laminar case, the streamwise and spanwise discretizations are irrelevant since those terms cancel out in the governing equations). At the vertical boundary, a zero-gradient condition is applied (i.e. $\partial u_1 / \partial x_3 = 0$).

Each simulation was run for 100 periods T until a quasi-steady state was reached. We assume that the size of the domain and this spin-up time are both sufficiently large as to have negligible effects on the results (for high resolutions these assumptions may be less valid). Table I gives a summary of the numerical parameters. The maximum error in the horizontal velocity after 100 periods of oscillation, as compared with the above analytical solution, was calculated as a measure of the numerical accuracy of the NS-LES simulations:

$$\varepsilon = \max[u_1(x_3, t = 100T) - u_{a1}(\omega t = 0)]. \tag{45}$$

While there are many numerical parameters affecting NS-LES simulations, for this idealized laminar oscillatory BL problem, all other things being equal, only two are significant: the vertical grid spacing Δx_3 and time step Δt. Indeed, for this case, the governing equations reduce to a 1D problem where the viscous term (computed with second-order center differencing) is integrated in time (with the second-order Adams–Moulton method). Thus, we expect that as long as we use a small enough time step and/or the BL is sufficiently (vertically) resolved, the numerical

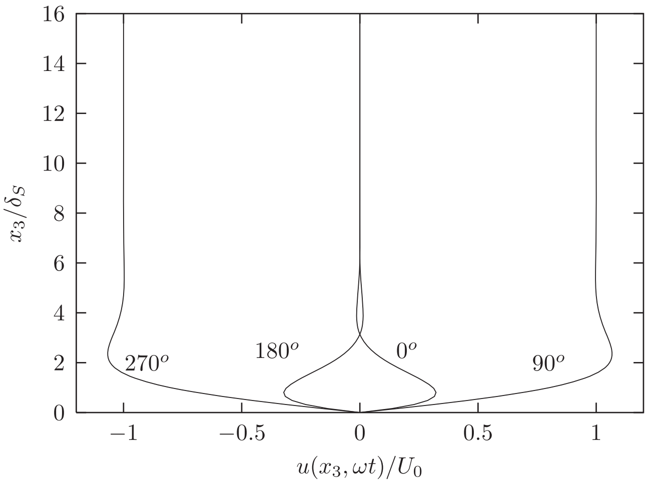

Figure 3. Stokes second problem for an oscillatory laminar BL flow. Analytical solution for the vertical variation of the horizontal velocity, u_{a1}, for different phases of oscillations.

error ε should show a second-order reduction with either grid size or time step. This is verified in Figure 4, for computations performed using a very small time step, $\Delta t = 0.001T$, and grid size $\Delta x_3 = \delta_S/32$ to δ_S, and in Figure 5 where a small grid size, $\Delta x_3 = \delta_S/64$, is used and time step varies from $\Delta t = 0.01 - 0.2T$. The expected second-order convergence is obtained when neither of the governing parameters is too small or too large. When time step or grid size was very large, the model did not resolve the BL oscillations well, and when the time step was very small, errors were dependent mostly on grid size. For (unnecessarily) very small time step and grid size, the error increased slightly as compared with the expected convergence, likely due to round-off and truncation errors.

4.1.2. Steady streaming. The next validation test of the implementation of the perturbation approach in the NS-LES solver is also for a laminar wave-induced BL, which unlike the previous application is forced by a time- and space-varying inviscid velocity, representing an incident linear Stokes wave. This results in an additional test of the convection terms in the model. The inviscid forcing is analytically defined from linear wave theory as [29]

$$u_1^I = \frac{Hgk}{2\omega}\frac{\cosh(k(x_3-h))}{\cosh kh}\cos(kx_1-\omega t) \tag{46}$$

$$u_2^I = 0 \tag{47}$$

Table I. Parameters for laminar oscillatory BL simulations in NS-LES model.

Domain height	$16\delta_S$
Upper boundary condition	Zero-gradient
Wall boundary condition	No-slip
Initial conditions	$u_i^P(x_i, t=0) = 0$
Simulation spin-up time	$100T$
Forcing	$u_1^I(t) = U_0 \sin\omega t,\ u_2^I = u_3^I = 0$
Free-stream velocity	$U_0 = \pi$
Forcing period	$T = 1$
Kinematic viscosity	$\nu = \pi$
Stokes length	$\delta_S = 1$
Reynolds number	$Re_\delta = 1$

Note: The results are independent of horizontal parameters.

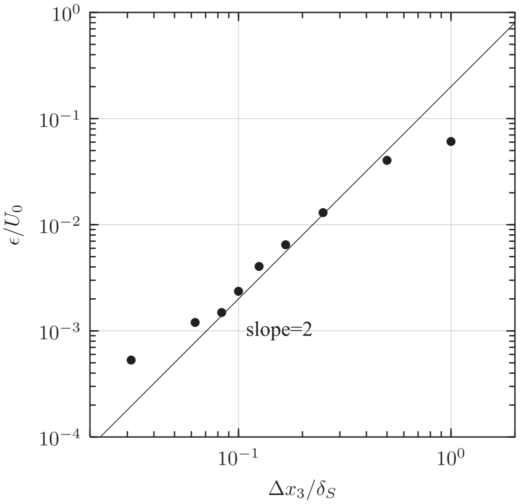

Figure 4. Maximum numerical error of NS-LES for velocity in an oscillatory laminar BL (with $Re_\delta = 1$), as a function of grid size for $\Delta t/T = 0.001$.

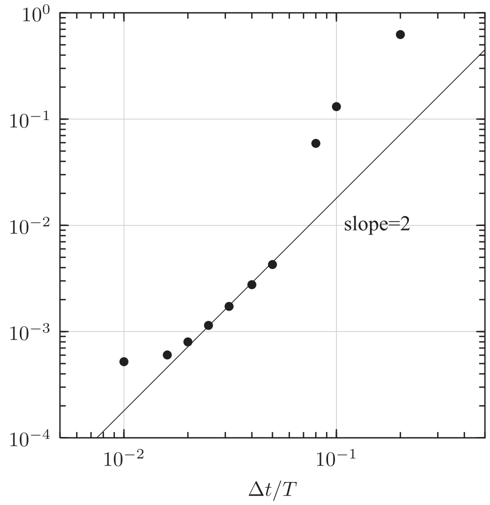

Figure 5. Maximum numerical error of NS-LES for velocity in an oscillatory laminar BL (with $Re_\delta = 1$), as a function of time step for $\Delta x_3 = \delta_S/64$.

$$u_3^I = \frac{Hgk}{2\omega}\frac{\sinh(k(x_3 - h))}{\cosh kh}\sin(kx_1 - \omega t) \tag{48}$$

for a wave height H and angular frequency ω, in depth h, and wavenumber k given by the dispersion relationship: $\omega^2/g = k\tanh kh$. In this case, rather than solving for the perturbation pressure to enforce mass conservation, we note that near the bottom, $u_3(x_1, x_3, t) \ll u_1(x_1, x_3, t)$, so that we can ignore the vertical momentum equation in the BL and instead compute the vertical velocity from the mean mass conservation (note, here again the turbulent fluctuations are zero so: $\bar{u}_i^P = u_i^P$):

$$\bar{u}_3^P(x_1, x_3) = -\int_0^{x_3} \frac{\partial \bar{u}_1^P}{\partial x_1}(x_1, x_3')\,\mathrm{d}x_3' \tag{49}$$

Because this bypasses the Poisson equation solver, that is normally used in the NS code to calculate pressure, the computational speed is dramatically increased. However, the solution produced here would be equivalent to that found using the full NS equation solver, assuming a correct pressure boundary condition is specified.

Longuet-Higgins [49] was the first to show the occurrence of and calculate the mean (i.e. period-averaged) mass transport velocity $\langle u \rangle$ (i.e. steady streaming) induced in the oscillatory BL under progressive waves, in the direction of wave propagation. This velocity occurs even when the forcing is specified from linear wave theory (note, additional contributions to the steady streaming velocity can also be result from nonlinear effects such as Stokes drift or from wave asymmetry). Thus, Longuet-Higgins found the linear Eulerian drift as:

$$\langle u \rangle = \frac{k\omega H^2}{4\sinh^2 kh}\left[\frac{3}{4} - \mathrm{e}^{-\xi}\cos\xi + \frac{1}{2}\mathrm{e}^{-\xi}\sin\xi + \frac{1}{4}\mathrm{e}^{-2\xi} - \frac{1}{2}\xi\mathrm{e}^{-\xi}\cos\xi - \frac{1}{2}\xi\mathrm{e}^{-\xi}\sin\xi\right] \tag{50}$$

where $\xi = (x_3 - h)/\delta_S$ [50, 87].

In this application, we computed the steady streaming in the laminar regime, i.e. using the LES with no eddy viscosity, starting with waves of height $H = 0.46\,\mathrm{m}$, period $T = 6\,\mathrm{s}$, in depth $h = 5\,\mathrm{m}$ (which is incidentally the conditions from an example used by Myrhaug and Holmedal [57]). We initially used a grid of 128 points in both streamwise (horizontal) and vertical directions (again, for this 2D laminar case, the spanwise direction is irrelevant), and a time step $\Delta t = T/256$. With this data, the spatial grid covered one wavelength $\lambda = 2\pi/k$ in horizontal by $16\delta_S$ in vertical direction. Periodic boundary conditions were specified in the horizontal directions and a no-slip condition on the bed. The results in Figure 6 for this case show that the calculated vertical profile of the Eulerian drift velocity agrees very well with the theoretical equation (50).

Convergence of the numerical solution is further assessed for this case, by varying the vertical grid size and calculating the difference between the steady streaming velocity for the highest point in the domain over the bed, u_∞ versus the theoretical solution of $(3k\omega H^2)/(16\sinh^2 kh)$, obtained by setting $x_3 \to \infty$ in Equation (50). Figure 7 shows that this error significantly and linearly reduces when the number of vertical grid points is varied from 16 to 128. Additional numerical accuracy and convergence tests are performed for oscillatory BL flows under different types of waves in the following sections.

4.1.3. Open boundary conditions. In earlier simulations of near-bed wave-induced flows (e.g. [14]), a boundary condition of the type $\partial u_i/\partial n = 0$ was used to simulate open boundary conditions on the lateral boundaries of the NS domain. Although not needed for the present periodic forcing, such conditions are tested in the present application, rather than periodic conditions as done so far, as these will allow simulating arbitrary rather than idealized incident waves in later applications. Additionally, correctly predicting steady streaming is key in wave-induced BLs, and thus we investigate the effect of this boundary condition on the simulated streaming velocities.

In the present perturbation approach, the open boundary condition for the horizontal velocity reads as: $\partial u_1^P/\partial n = 0$, which is exact for a spatially uniform oscillatory BL, but not for a wave-induced BL. We test the effect of this condition by running a test similar to that in the previous section, but varying the domain length with respect to the incident wavelength: L_1/λ. In order to keep Δx_1 constant and thus not to affect the discretization error, the number of grid points is adjusted at the same time. Because we want to consider several orders of magnitude, we will separately consider the case where $L_1 > \lambda$ (Figure 8) and $L_1 < \lambda$ (Figure 9). For the larger

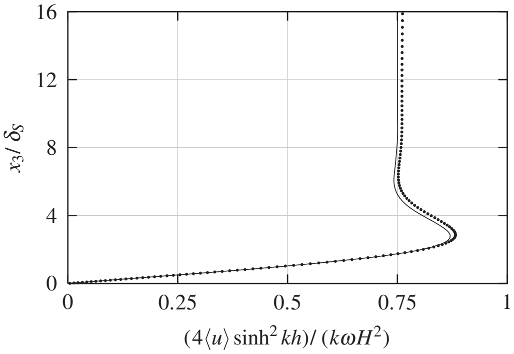

Figure 6. Vertical profile of non-dimensional Eulerian drift velocity, in a laminar oscillatory BL forced by linear Stokes waves, computed in NS-LES model (·) using a 128×128 grid, versus Longuet-Higgins [50] theory (—).

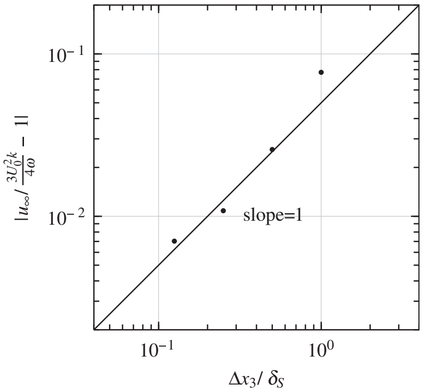

Figure 7. Same application and physical data as in Figure 6. Error (relative to the theoretical solution) of far-field ($x_3 \to \infty$) Eulerian streaming velocity as a function of vertical grid size.

DOI: 10.1002/fld

domains, we use $\Delta x_1 = \lambda/32$, and $L_1 = \lambda, 2\lambda, \ldots, 2^4\lambda$, and for the smaller domains, $\Delta x_1 = \lambda/256$, and $L_1 = \lambda, \lambda/2, \ldots, \lambda/2^4$.

The results in the figures show that when applying a simple free gradient boundary condition for the horizontal velocity, we achieve similarly good results for steady streaming velocities, as when using a periodic condition, a quarter-wavelength from the edge of the domain. This condition is thus reasonably successful, as long as the NS domain is about a wavelength across. Simulating steady streaming in smaller domains would most likely require more sophisticated boundary conditions.

4.1.4. Eulerian drift in near-breaking waves. While we have so far only considered BL forcing from linear waves, with one set of parameters, a variety of more realistic forcings can be used in the coupled model. This is illustrated by calculating the Eulerian BL drift for FNPF waves shoaling over a sloping bed, in a setup similar to that of Figure 2.

To reduce the computational cost, laminar flow conditions were selected in these simulations. Indeed, the number of grid points required in the model, in each direction (i.e. N_1, N_2, N_3), is a function of flow conditions. For the laminar wave-induced BL case, one only needs to resolve a single wavelength (e.g. $N_1 = O(10^2)$), the lateral direction is unimportant (e.g. $N_2 = O(10^0)$), and the BL needs to be resolved (e.g. $N_3 = O(10^2)$); hence, the total number of points is $O(10^4)$. By contrast, for a turbulent oscillatory BL (such as in the last application in the following section), the lateral direction is important for resolving 3D eddies (e.g. $N_2 = O(10^2)$), and in the streamwise direction it is the eddies which must be resolved, not the wavelength of a wave, but again, $N_1 = O(10^2)$, so the total number of grid points is $O(10^6)$. The present wave-induced BL case is more computationally intensive than the idealized oscillatory flow specified in the last application,

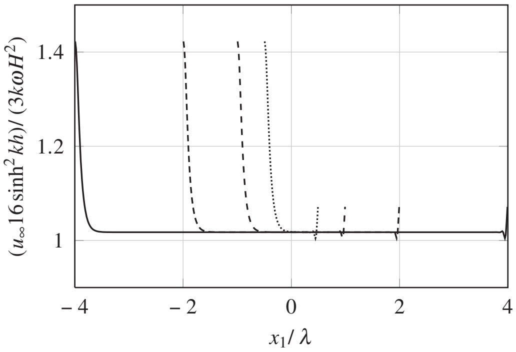

Figure 8. Same application and physical data as in Figure 6. Non-dimensional far-field Eulerian streaming velocity, in a laminar oscillatory BL forced by linear Stokes waves, computed in NS-LES model (various lines) versus theory (converged value of nearly 1), using open boundary conditions, for domains of length 8λ (—), 4λ (– –), 2λ (- -), and λ (···).

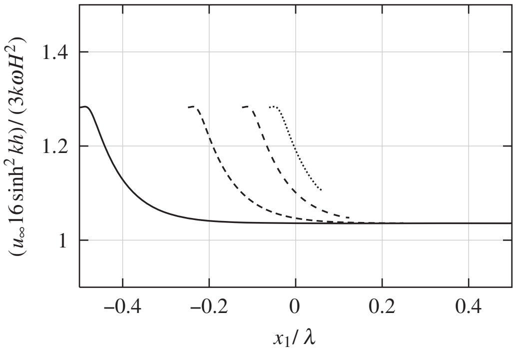

Figure 9. Same application and physical data as in Figure 6 and same test as in Figure 8 for domains of length λ (—), $\lambda/2$ (– –), $\lambda/4$ (- -), and $\lambda/8$ (···).

because hundreds of wave periods are needed in order for the steady streaming velocity to converge (a second-order effect), whereas for the oscillatory BL, only 10 oscillations or so are used. Because of the vast difference in the size of eddies in the BL and a typical wavelength, the computational domain required for a turbulent wave-induced BL would be larger than both (e.g. $N_1 = O(10^4)$; $N_2 = O(10^2)$; $N_3 = O(10^2)$), resulting in a domain with perhaps $O(10^8)$ grid points. Additionally, the simulation would have to be run for hundreds of periods as well, resulting in a computational time several orders of magnitude longer than for results shown here.

Another feature of the present simulations (Table II) is that 'numerically exact' FNPF periodic waves are generated in the NWT, instead of approximate periodic waves, such as generated by a sinusoidally moving piston or flap wavemaker (as in laboratory wave generation). Specifically, we use the zero mean-flux streamfunction wave generation proposed by Grilli and Horrillo [5], to generate a wave of period $T = 2.5\,\text{s}$ and height $H = 0.175\,\text{m}$ in an NWT of 'offshore' depth $h_o = 1\,\text{m}$, which extends over 40 m (Figure 2). This method was developed to generate nonlinear waves in an NWT, whose nonlinear Stokes drift is canceled by specifying a current equal and opposite to the wave mean mass flux. This both prevents the tank mean water level from artificially increasing and allows for the undertow current generated in the nearshore part of the tank to 'exit' through the tank offshore boundary.

To cause wave shoaling, a slope $s = 1/24$ is specified in the NWT starting at 5 m from the wavemaking boundary. To prevent wave overturning and breaking (which would interrupt FNPF computations), the water depth levels off at 20 m from the wavemaker, at a depth of 0.375 m, and then increases to $h_1 = 0.5\,\text{m}$ in the absorbing beach (AB), following a hyperbolic tangent similar to the increase of the damping coefficient in the AB; this causes wave de-shoaling and makes it easier for the AB to absorb the incident wave energy. The NWT boundary is discretized with 513 nodes, with a grid spacing on all boundaries of approximately 0.16 m. Along the surface, the boundary is discretized with 249 mixed cubic interpolation (MCI, [4]) elements. On the wavemaker, bottom, and absorbing piston of the NWT, the boundary is discretized with 3, 125, and 2 three-node cubic elements, respectively. In order to force the oscillatory BL to be laminar (see Figure 1), a kinematic viscosity of $1 \times 10^{-5}\,\text{m/s}^2$ is assumed.

In order to obtain highly nonlinear physics related to shoaling (e.g. with both trough/crest and rear/front wave asymmetry), the coupled NS-LES domain had to be located very close to the theoretical breaking point for the selected sloping bed geometry. Even with the AB starting at the end of the sloping bed, it was observed that the absorption distance was not sufficient to prevent large nonlinear waves from forming a small scale overturning jet, due to the Lagrangian motion of the NWT nodes/water particles that caused node convergence in the wave crest area. The act of regridding free surface nodes at equal arc length intervals at every time step in combination with the AB, appeared sufficient to prevent hydrodynamic instabilities from causing waves to overturn.

The inviscid flow forcing for the NS-LES domain, encompassing the BL, is obtained using the approximation from Equations (40) to (42), from velocities computed at 32 wave gages (Figure 10). Note that the Stokes BL thickness is several orders of magnitude smaller than the water depth in the NWT, so the approximation using inviscid seabed velocities seems quite reasonable. [Note, inviscid velocities could be calculated at internal points within the NS-LES domain; however because the BL is so thin in this application, any vertical variation in such velocities would be

Table II. NWT parameters for example of steady streaming of near-breaking waves on a sloping bed.

Domain	Value
Wave period (T)	2.5 s
Initial wave height (H_0)	0.175 m
Forcing	Stream function wave
Time step (Δt)	0.025 s
Slope (m)	1/24
Simulation time	$25T$
Number of wave gages	38
Wave gage locations (x_{g1})	From 10.375 to 19.625 m, spaced evenly

more likely caused by numerical errors than any physical variation; similarly, the velocity gradient is computed with finite differences but this could be made more accurate using the NWT boundary integral equation.]

The inviscid forcing is ramp-up by running the NWT for an initial 25 wave periods, and is then used to force the NS solver. To do so, the final wave period of NWT simulations is repeated from then on, to provide a quasi-periodic forcing. This assumes that the NWT has reached a quasi-periodic state by then, which is demonstrated, e.g. in Figure 11.

For each test, we use a moderately coarse NS grid of 32×32 $(L\times H)$ points, with 100 time steps per period (Table III). The NS domain is 8 m long (from 11 to 19 m from the wavemaker; Figure 11), 4.5 cm thick, and the simulations are run for 1000 wave periods. [The domain was specified with two points in the lateral direction, with a width of 10 cm, although this is presumed to be unimportant for this laminar case.] In general, a streaming velocity away from the beach was observed (Figure 12), with significant variation across the domain. Interestingly, the trend of

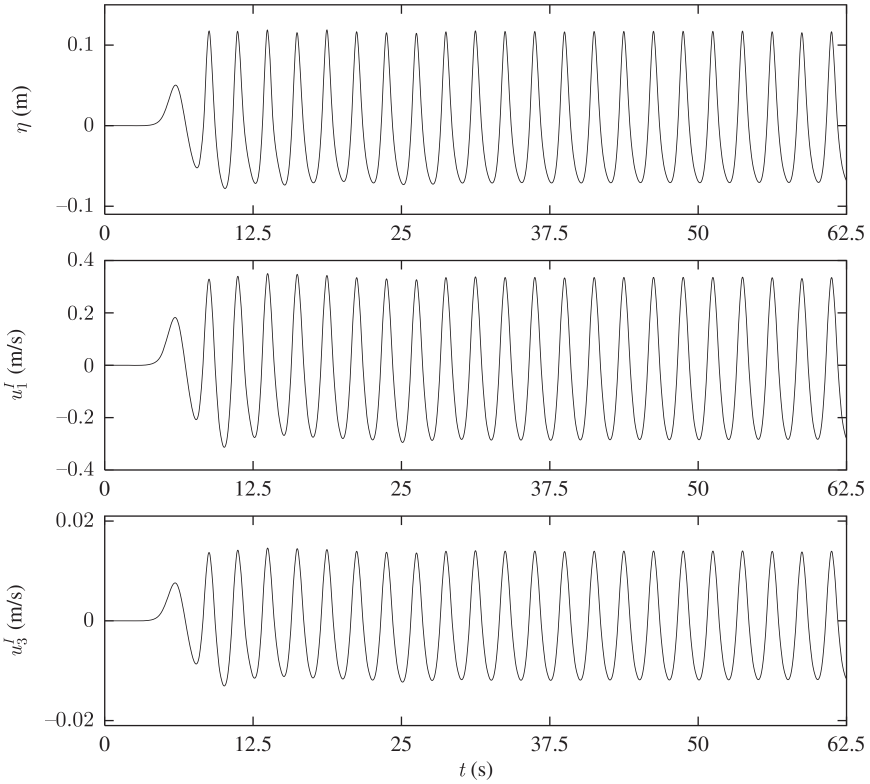

Figure 10. Example of surface elevation, and horizontal/vertical velocity components simulated at the NWT seabed (—), 15 m from the wavemaker (averaging the results at adjacent wave gages at 14.875 and 15.125 m).

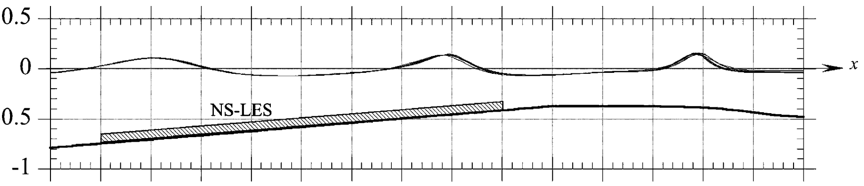

Figure 11. Free surface elevation predicted by NWT around the area of interest (from 11 to 19 m from the wavemaker, with overlapping data from 5 to $21T$ every two periods. [Vertical exaggeration is $2x$.] The NS-LES domain is sketched for information.

larger offshore mean current in deeper water just outside the BL is reversed very near the seabed (Figure 13). Note that others (e.g. Myrhaug and Holmedal [57]) have also found that adding the second-order component of a Stokes wave results in a weaker mean onshore than that predicted by Longuet-Higgins theory or even an offshore Eulerian steady streaming, as shown here. [One possible mechanism for the reversal of the drift velocity direction is the generation of an offshore undertow current, due to the impermeable boundary condition on the right side of the NWT.]

While these results show that the coupled numerical model works as intended and can produce relevant results for realistic incident waves, applicable to actual wave-induced BLs, a final

Table III. NS-LES solver parameters for the steady streaming of near-breaking waves on a sloping bed.

Domain	Value
$L_1 \times L_2 \times L_3$	$8\,\mathrm{m} \times 0.1\,\mathrm{m} \times 0.045\,\mathrm{m}$
$N_1 \times N_2 \times N_3$	$32 \times 2 \times 32$
Upper boundary condition	Zero-gradient
Wall boundary condition	No-slip
Initial conditions	$u(x_i, t=0)=0$
Time step (Δt)	0.025 s
Viscosity (ν)	$10^{-5}\,\mathrm{m}^2/\mathrm{s}$
Simulation time	2502.5 s

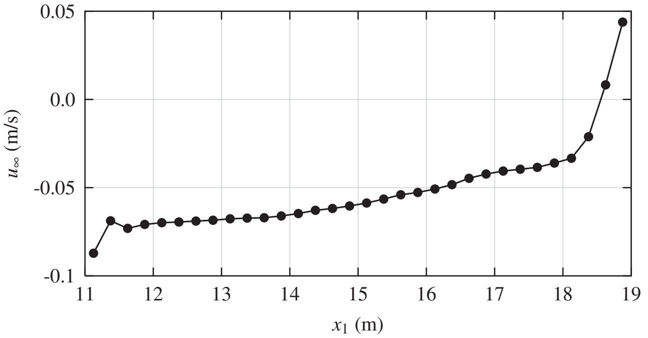

Figure 12. Eulerian drift at the edge of the boundary layer predicted by Navier–Stokes solver for fully nonlinear potential flow forcing.

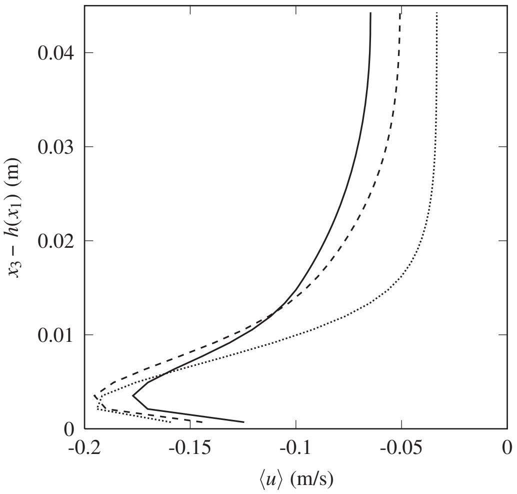

Figure 13. Time-averaged Eulerian drift profiles (versus distance off seabed) predicted by Navier–Stokes solver for fully nonlinear potential flow forcing at $x=13.125\,\mathrm{m}$ (—), $x=15.125\,\mathrm{m}$ (– –), and $x=17.125\,\mathrm{m}$ ($\cdots$)).

demonstration is required to show that the SGS models implemented in the LES are adequate to reproduce the desired turbulent flow properties. This is done in the following section.

4.2. Turbulent oscillatory boundary layers

We next validate the LES for turbulent oscillatory BLs. We choose a uniform oscillatory flow because of the lack of sufficiently detailed experimental data for more complex wave-induced flows. To compare results with the laboratory experiments of Jensen et al's [43], which were performed in an oscillatory flume (U-tube), the model inviscid forcing was selected similarly to the initial laminar BL test cases, as a vertically uniform oscillatory flow (see Equation (43)), with velocity amplitude U_o and period T ($\omega = 2\pi/T$). Jensen *et al.*'s experiments consisted in 15 different test cases, of which we selected for comparison two cases with a rough bed: nos. 12 and 13 (see physical data in Table IV). In each case, the mean velocity and Reynolds stresses were measured as a function of time and elevation over the rough bed in the BL.

To achieve good accuracy and resolution in simulated results and also to ensure that the number of 'samples' used for ensemble averaging is large enough, a NS grid size of $128 \times 32 \times 64$ is used in simulations (see numerical parameters in Table V), slightly larger than that used by Radhakrishnan and Piomelli [27] who recently reported on similar comparisons. Note, for very simple flows such as considered here, this need for performing averaging operations is one disadvantage of NS-LES models as compared with an RANS model, which directly compute mean quantities.

4.2.1. Wall stress and mean velocity. Jensen *et al.* did not measure wall stress $\langle \tau_w \rangle$, but rather (for test #13 only) they did measure a time-series of the mean streamwise velocity at a very small height over the wall, $x_3 = 0.0006\,A$ (relative to the amplitude of oscillation $A = U_0/\omega$; equivalent to a height x_3 of 1.86 mm), which we used together with a log-law assumption, to predict wall stress. Figures 14 and 15 show wall stress computed for tests #12 and #13, using the three SGS

Table IV. Parameters (period T, free-stream maximum velocity U_0, viscosity ν, Nikuradse roughness k_s, and free-stream amplitude A) for selected laboratory experiments of turbulent oscillatory BLs [43] used for comparison with numerical simulations.

Test no.	T (s)	U_0 (m/s)	ν (m^2/s)	Re	k_s (mm)	A/k_s
12	9.72	1.02	1.14×10^{-6}	1.6×10^6	0.84	1800
13	9.72	2.00	1.14×10^{-6}	6.0×10^6	0.84	3700

Table V. Parameters for numerical simulations of turbulent oscillatory BLs.

Domain	Value
$L_1 \times L_2 \times L_3$	$636.3\delta_S \times 318.2\delta_S \times 100\delta_S$
$N_1 \times N_2 \times N_3$	$128 \times 64 \times 32$
Grid discretization (Smagorinsky SGS model)	Uniform grid spacing
Grid discretization (dynamic SGS models)	Vertical exponential stretching with ratio 1.1 Minimum grid height: 0.93 mm Aspect ratio at wall: 10:1:10
Upper boundary condition	Zero-gradient
Wall boundary condition	Log-layer approximation
Wall roughness	$z_0 = 2.8 \times 10^{-5}$ m
Initial conditions	$u(x_i, t = 0) = 0$
Simulation spin-up time	$5T$
Forcing	$u_1^I(t) = U_0 \sin \omega t$
Δt	$T/4860$ (test 12) or $T/9720$ (test 13)
Simulation time	$10T$
Output sampling frequency	Every $T/12$

DOI: 10.1002/fld

models in the NS-LES; in the latter test, this is compared with experimental values inferred from near-wall velocity measurements.

Wall stress is qualitatively consistent among the three SGS turbulence models used. Additionally, for test #13, numerical results with the DSM and DMM approaches agree well both with each other and with experiments, while these are underpredicted by the Smagorinsky model; a better agreement for the latter could probably be achieved by calibrating the Smagorinsky coefficient. Note that while of the DSM and DMM approaches show a good performance, they rely on the enhanced eddy viscosity near the wall, which tends towards the mixing-length approximation. A time-invariant eddy viscosity distribution proportional to the height above the wall was found by Grant and Madsen [31] to produce good results for both wall stress and mean flow, thus it is reasonable to expect that the DSM and DMM approaches would also be successful.

The results in Figures 16 and 17 show that model results for the mean flow velocity, $\langle u_1 \rangle$, are again qualitatively consistent among the three SGS turbulence models used, with the Smagorinsky approach underestimating the BL thickness. Numerical results using DSM or DMM agree well with experiments, for both the #12 and 13 test cases, at six selected phases of the flow, over half a period of oscillation.

4.2.2. Turbulent intensity and Reynolds stress. For both test cases #12 and 13, we calculated the streamwise turbulent intensity $\langle u_1'^2 \rangle^{1/2}$ (Figures 18 and 19), the vertical (wall normal) turbulent intensity $\langle u_3'^2 \rangle^{1/2}$ (Figures 20 and 21), and the Reynolds stresses $\langle u_1' u_3' \rangle$ (Figures 22 and 23), and compared those to experiments. The figures show a good agreement of all model results with experiments when using DSM or DMM, but not so with the Smagorinsky model. In particular, for test #12, at the lower Reynolds number, the Smagorinsky approach fails to produce much resolved turbulence. This highlights the significance of having to tune this model's coefficient to different flow conditions.

Near the wall, all simulation results underpredict the experimental turbulence intensity. For the constant coefficient Smagorinsky model, this is expected because this model is known to

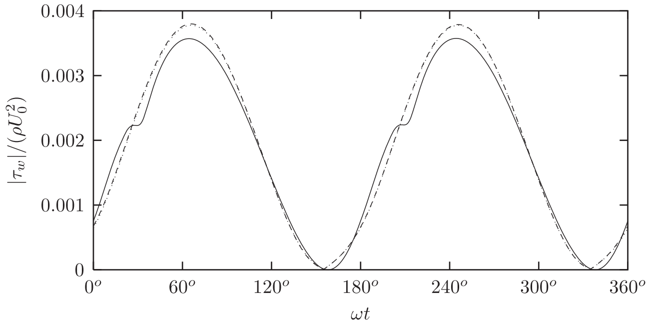

Figure 14. Numerical simulations of turbulent oscillatory BL: mean wall stress, $\langle \tau_w \rangle$ (determined by log-law) as a function of phase angle for conditions of test #12 [43] with different SGS models: (—) Smagorinsky; (– –) dynamic Smagorinsky; and (···) DMM.

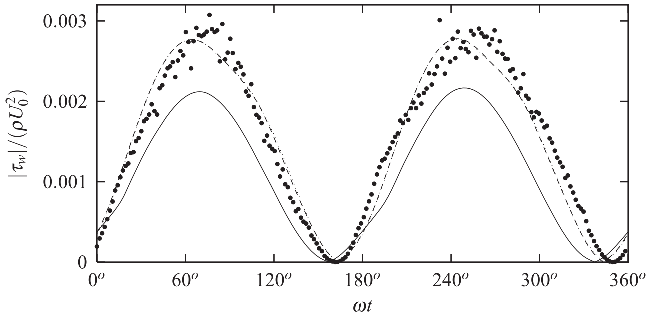

Figure 15. Same case as Figure 14, for test #13, with comparison to experiments (●).

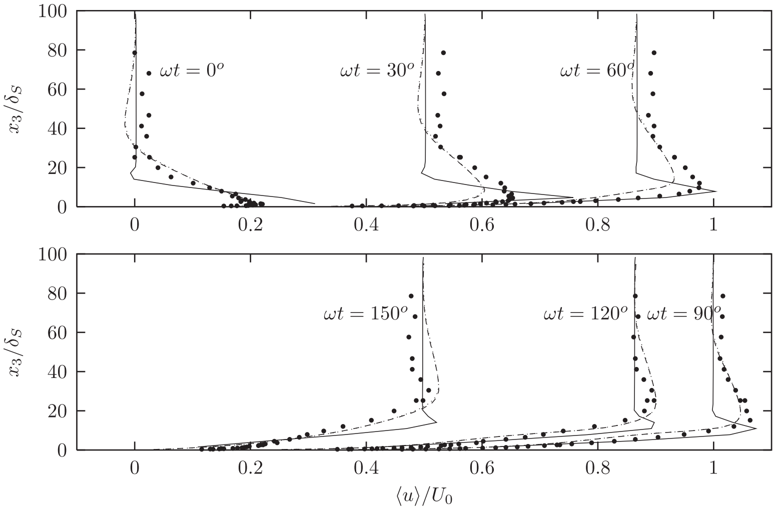

Figure 16. Same case as Figure 14. Mean streamwise velocity profiles, $\langle u_1\rangle$, for test #12.

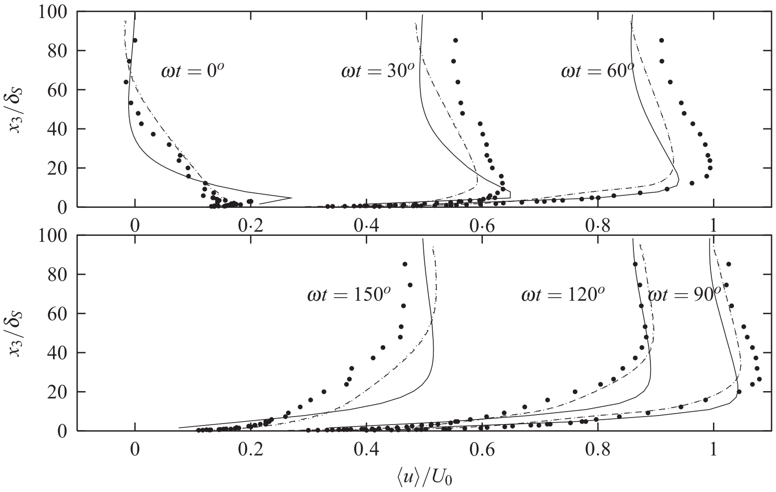

Figure 17. Same case as Figure 14. Mean streamwise velocity profiles, $\langle u_1\rangle$, for test #13.

overpredict near-wall dissipation. For the dynamic models, the underpredicted turbulent intensity is more likely due to the grid aspect ratio near the wall. The vertical stretching of the grid results in 'pancake'-like grid cells, which are significantly wider in the streamwise and spanwise directions than in the wall-normal direction. The typical eddy size, however, is of similar size in all directions, and so the implicit grid-scale filter averages over many eddies in a way similar to a RANS ensemble average. The most similar numerical study to the present one is the LES work of Radhakrishnan and Piomelli [27], which studied test case #13. Their results for the near-wall turbulent intensity are similar to ours for most phases of the oscillation, although Radhakrishnan and Piomelli did obtain a better agreement with experiments at $\omega t = 60^\circ$ and $\omega t = 90^\circ$, albeit using different SGS models, and without having the large aspect ratio for the grid cells near the wall.

Far from the wall, there is an occasional underprediction of the turbulent intensity. Other numerical studies have reported this problem as well, which Mellor [39] suggests is an experimental artifact. The amplitude of the oscillation for test #13 is 3.1 m, so a fluid particle can move as far as 6.2 m over the course of each oscillation. Hence, at the end of each period (i.e. around 0°), some of the fluid being measured may have a half-period earlier been outside of the 10 m straight

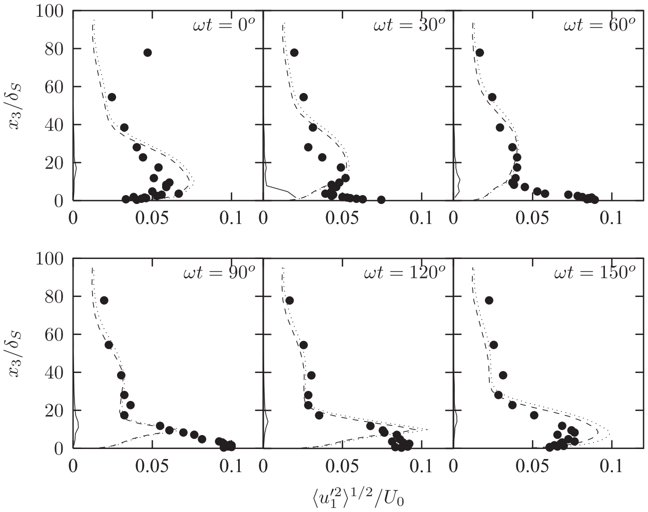

Figure 18. Streamwise turbulent intensity, $\langle u_1'^2\rangle^{1/2}$, for test #12.

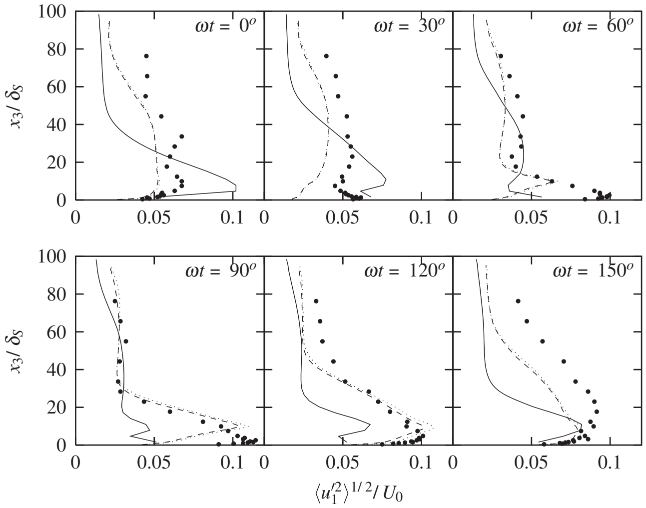

Figure 19. Streamwise turbulent intensity, $\langle u_1'^2\rangle^{1/2}$, for test #13.

test section of the oscillatory water tunnel used in experiments. Although Jensen *et al.* took some additional measurements to attempt to show that this would have no effect, it does seem to explain the outlier seen at the 0° phase angle (e.g. Figure 18). The results far from the wall are similar to others (e.g. Radhakrishnan and Piomelli), although our turbulent intensities match experiment somewhat better far from the wall at phases 0° and 30°.

In some cases, the size of the discretization may prove to be the limiting factor. For case #13, for instance, the Reynolds stress at 90° was experimentally measured to be maximum at $2.6\delta_S$ over the bed (Figure 23), whereas the first grid cell is 3 δ_S high. Important physics may not be properly modeled as a result. Note that Sleath [48] found that the Reynolds stress is a minor contributor to the shear stress. As a result, one would expect that the vertical momentum flux would be governed more by the periodic velocity components than the turbulent momentum flux, and thus more study would be required to verify whether resolving this peak in Reynolds stress is important for the numerical simulations.

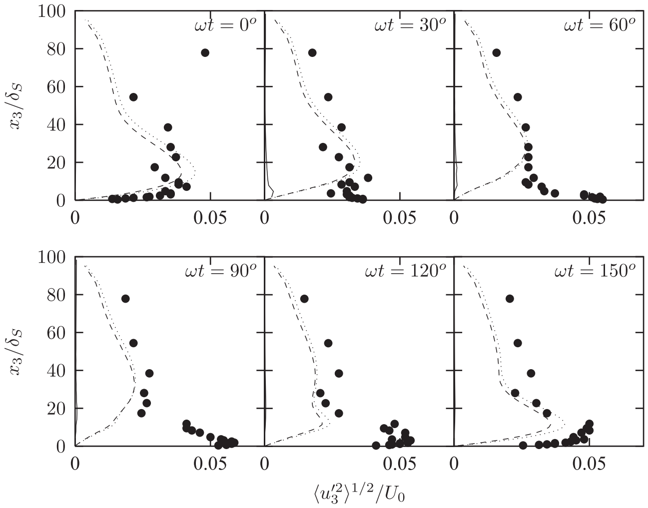

Figure 20. Wall normal turbulent intensity, $\langle u_3'^2\rangle^{1/2}$, for test #12.

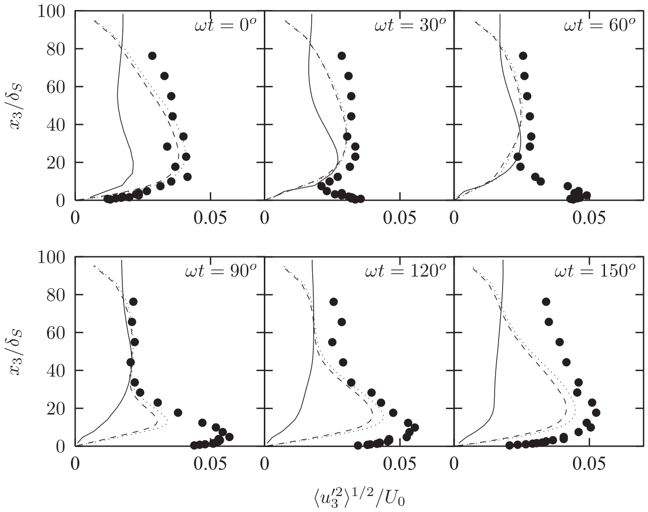

Figure 21. Wall normal turbulent intensity, $\langle u_3'^2\rangle^{1/2}$, for test #13.

4.2.3. Velocity spectra. In addition to examining second-order turbulence statistics, we analyzed velocity spectra, such as the streamwise velocity fluctuation spectrum, which can be defined as the discrete Fourier transform:

$$E_{11}(k_1) = \left| \sum_{n=1}^{N_i} [u_1]_{n,j,k} \mathrm{e}^{-2\pi i n k_x / N_i} \right| \tag{51}$$

and can also be phase-averaged. Note, such spectra are computed directly from the resolved velocities at each grid point, and thus develop as a result of simulations. It should be stressed that the numerical method is not a spectral method and, hence, spectra are not *a priori* assumed in the SGS models used here.

Figure 24, for instance, shows the phase-averaged spatial velocity power spectra for the DSM test #13 run at 0°. We are able to see at least what appears to be the inertial subrange in the spectral results (slope 5/3). Note that the spectra are not smooth lines, but somewhat stochastic. This indicates that the scale of the largest vortex structures is not well resolved, which is somewhat expected because particles in the free-stream oscillate horizontally over $2A = 2U_0/\omega \approx 6.2\,\mathrm{m}$,

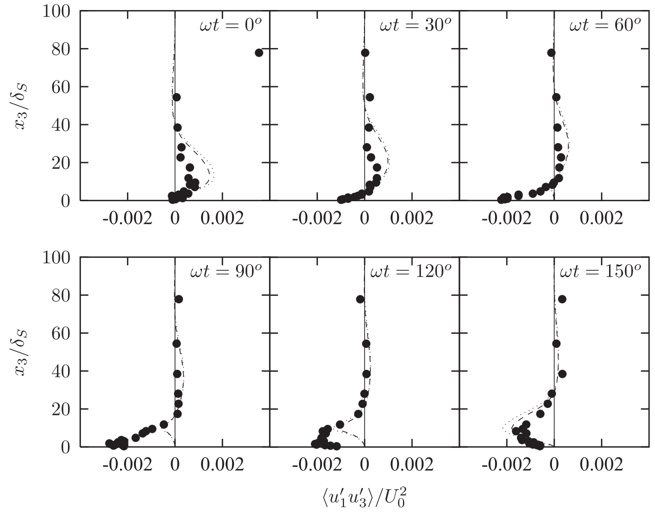

Figure 22. Reynolds stress, $\langle u'_1 u'_3 \rangle$, for test #12.

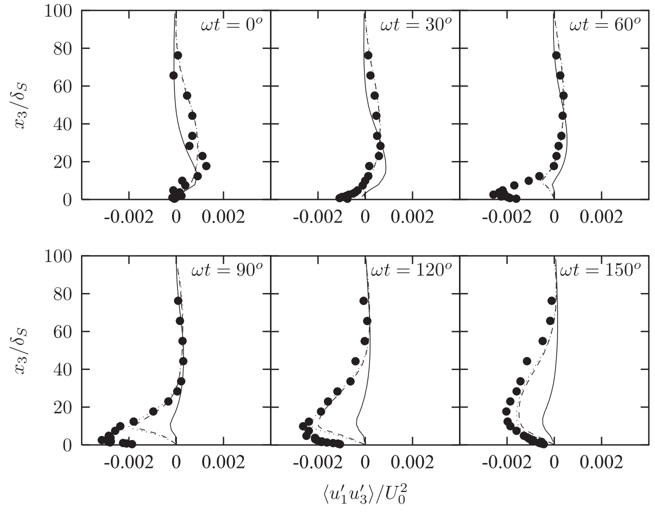

Figure 23. Reynolds stress, $\langle u'_1 u'_3 \rangle$, for test #13.

whereas the computational domain is approximately an eighth of that size. A similar problem was encountered by Costamagna *et al.* [88], but because the Jensen *et al.* data is for fully turbulent conditions, we may use phase-averaging (i.e. averaging the data for the same phase from different oscillations) in order to smooth results, as we have done above. Because the dynamics is mostly controlled by the near-wall behavior (where the eddies are smaller), the largest scales are unlikely to be particularly important, but future studies should consider using larger computational domains to verify this claim.

4.2.4. Two-point spatial correlation. One premise of the modeling of turbulent flows in 'infinitely long' oscillatory BLs, using a finite length spatially periodic domain, is that there is no correlation between the velocity fluctuations a half-domain away (see, e.g. [1]). This will be achieved provided the domain size is large enough, which can be a posteriori verified in numerical results by calculating and verifying that the two-point spatial autocorrelation of the perturbation velocity field is nearly zero, between points half a domain away in the horizontal direction.

Figure 25 shows the autocorrelation of each of the three components of the velocity fluctuations in both the streamwise and spanwise directions at a given height for the DSM run of test 13. The

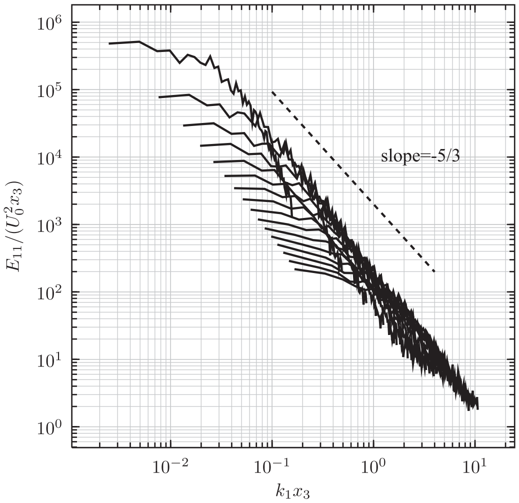

Figure 24. Non-dimensional velocity spectra for the resolved streamwise velocity field.

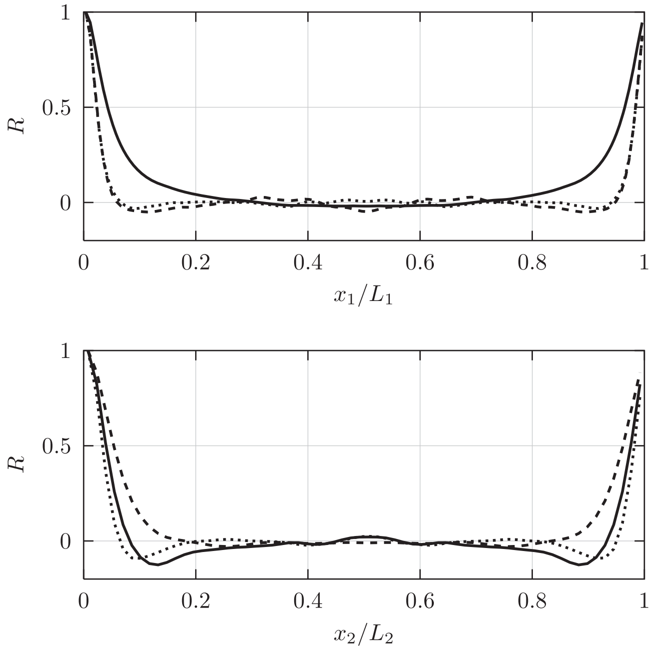

Figure 25. Two-point spatial autocorrelation functions for the component velocity fluctuations, u_1' (—), u_2' (– –), u_3' ($\cdots$), at the first gridpoint above the rough bed, as a function of distance for test case #13, in both the streamwise direction (averaged over the spanwise direction; upper panel) and spanwise direction (averaged over the streamwise direction; lower panel).

autocorrelation function is very small for much of the domain, in both streamwise and spanwise directions, indicating that the domain is large enough.

5. CONCLUSIONS

A perturbation approach to the NS equations was developed for simulating wave-induced BL flows, in a coupled model implementation, in which the NS domain is embedded within a fully nonlinear inviscid NWT. The NS equations are solved using an LES with a variety of SGS turbulence models. For many coastal engineering problems, the physics of waves is such that the flow is

DOI: 10.1002/fld

nearly irrotational in most of the fluid domain, except for thin free surface and bottom BLs. Hence, the region of the seafloor requiring full NS modeling may be relatively small, which justifies the coupled/hybrid approach and allows using efficient and relevant models for various parts or regions of the solution, based on the corresponding salient physics. Another advantage of the perturbation method is that the inviscid component of the flow fields (which is either analytical or obtained in the NWT) is not subject to the numerical errors of the NS solver.

The NS solver is first validated for simple laminar or turbulent oscillatory BL flows (for the former, the eddy viscosity was zero and the LES was bypassed). For laminar cases, the results are very close to theoretical closed-form solutions for oscillatory BLs, both in simple periodic flows or under linear wave forcing. Moreover, simulations demonstrate the expected rates of convergence to the exact solution, with both spatial and temporal discretizations. The hybrid NWT-NS model is then used to compute the steady streaming current due to fully nonlinear periodic waves, shoaling on a slope near the breaking point, which demonstrates the possibilities of the approach to simulate realistic nearshore wave processes. Simulations for rough turbulent oscillatory BL flows are finally performed, which favorably compared with experimental data, for both mean and turbulent fields.

More specifically, the results for 1D (i.e. forced by spatially uniform horizontal flows) laminar oscillatory BLs over a flat boundary showed the expected second-order convergence of numerical errors to the Stokes solution [86], in both space and time. This was to be expected from the published results, as all the modified terms in the new perturbed NS equations, as compared with the original Cui and Street work [22], were zero for this very simple test case. Similarly, good results were obtained for laminar oscillatory BLs induced by linear Stokes waves, which yield non-spatially uniform forcing flows. This case further tested the application of the inviscid forcing terms in the perturbation form of the momentum equations (i.e. nonlinear convective terms). In these simulations, we first used spatially periodic boundary conditions in both lateral directions of the NS domain and found that the computed steady streaming velocities in the BL closely matched those theoretically predicted by Longuet-Higgins [50]. Effects of using more general (gradient free) open boundary conditions were then tested in the case of wave forcing, and results were shown to be accurate within half a wavelength of the lateral boundaries of the NS domain.

Preliminary numerical tests of the fully coupled NWT-NS model were performed, for simple 'numerically exact' nonlinear periodic incident waves shoaling over a 1:24 slope. Specifically, we calculated fully nonlinear inviscid flow fields near the breaking point in the NWT, for periodic waves shoaling over a plane slope, and used those to force BL flows (limited to laminar cases) in a small embedded near-bottom NS-LES domain. Results show that for the selected parameters, unlike with the flat-bottom linear wave forcing case, the steady streaming in the BL is both stronger and directed offshore, with significant spatial variation.

Finally, for rough turbulent oscillatory BL flows, the LES model, with various SGS, was able to accurately predict measured mean flow fields, wall stress, and second-order turbulent statistics. Specifically, all results favorably compared with the experimental data of Jensen *et al.*'s test #12 and 13 [43] (except over small regions for the turbulent fields). Our simulations with dynamic SGS showed somewhat better agreement with the measured turbulent intensity far from the wall than the recent results of Radhakrishnan and Piomelli [27]. This may be partly due to using a gradient-free boundary condition, as opposed to setting the wall-normal velocity to zero in the free-stream, and to increased model accuracy when using the perturbation method.

While these experiments show that a hybrid NWT-LES can accurately determine turbulent characteristics of coastal flows, note that for turbulent BLs over complex 3D bathymetry, this technique may still be computationally demanding depending on the size of the domain. A LES of turbulent flow needs to simulate eddies which may be several orders of magnitude smaller than the size of the domain, in 3D (regardless of whether the driving force is uniform, or varies in one or more dimensions), and perhaps over several hundreds of wave periods to determine e.g. the induced steady streaming velocity. Limitations have existed for high-Reynolds laboratory measurements as well, however, and only recently has the wave-induced steady streaming velocity of a fully turbulent BL over sloping bed been made [89]. More complex applications should be made possible as computer performance increases.

DOI: 10.1002/fld

In future work, we will build on the model capabilities demonstrated in these initial somewhat idealized numerical applications, by simulating more general wave-induced turbulent BL flows. We will finally add a sub-model for sediment suspension and transport, with the eventual goal of being able to simulate wave-induced bed form development around objects on the seabed.

ACKNOWLEDGEMENTS

Both authors gratefully acknowledge support of grant Nb. N000140510068 from the US Office of Naval Research (ONR) Coastal Geosciences Division (code 321CG). In addition, the first author acknowledges support from an ONR-NDSEG fellowship. Prof. R. Street and Prof. O. Fringer are thanked for providing the initial LES code, and Dr Senthil Radhakrishnan is gratefully acknowledged for providing us with a copy of the Jensen *et al.* data.

REFERENCES

1. Moin P, Mahesh K. Direct numerical simulation: a tool in turbulence research. *Annual Review of Fluid Mechanics* 1998; **30**:539–578.
2. Deardorff JW. A numerical study of three-dimensional turbulent channel flow at large Reynolds numbers. *Journal of Fluid Mechanics* 1970; **41**(2):453–480.
3. Zang Y, Street RL, Koseff J. A non-staggered grid, fractional step method for the time-dependent incompressible Navier–Stokes equations in curvilinear coordinates. *Journal of Computational Physics* 1994; **114**(1):18–33.
4. Grilli ST, Subramanya R. Numerical modeling of wave breaking induced by fixed or moving boundaries. *Computational Mechanics* 1996; **17**:374–391.
5. Grilli ST, Horrillo J. Numerical generation and absorption of fully nonlinear periodic waves. *Journal of Engineering Mechanics* 1997; **123**(10):1060–1069.
6. Grilli ST, Voropayev S, Testik FY, Fernando HJS. Numerical modeling and experiments of wave shoaling over buried cylinders in sandy bottom. *Proceedings of the 13th Offshore and Polar Engineering Conference*, Honolulu, HI, 2003; 405–412.
7. Wei G, Kirby JT. A time-dependent numerical code for extended Boussinesq equations. *Journal of Waterway, Port, Coastal, and Ocean Engineering* 1995; **120**:251–261.
8. Wei G, Kirby JT, Grilli ST, Subramanya R. A fully nonlinear Boussinesq model for surface waves. I. Highly nonlinear, unsteady waves. *Journal of Fluid Mechanics* 1995; **294**:71–92.
9. Grilli ST. On the development and application of hybrid numerical models in nonlinear free surface hydrodynamics. In *Proceedings of the Eighth International Conference on Hydrodynamics*, Nantes, France, Ferrant P, Chen XB (eds). 2008; 21–50.
10. Guignard S, Grilli ST, Marcer R, Rey V. Computation of shoaling and breaking waves in nearshore areas by the coupling of BEM and VOF methods. *Proceedings of the 9th Offshore and Polar Engineering Conference*, vol. 3. Brest, France, 1999; 304–309.
11. Lachaume C, Biausser B, Grilli ST, Fraunie P, Guignard S. Modeling of breaking and post-breaking waves on slopes by coupling of BEM and VOF methods. *Proceedings of the 13th Offshore and Polar Engineering Conference*, Honolulu, HI, 2003; 353–359.
12. Biausser B, Grilli ST, Fraunie P, Marcer R. Numerical analysis of the internal kinematics and dynamics of three-dimensional breaking waves on slopes. *International Journal of Offshore and Polar Engineering* 2004; **14**(4):247–256.
13. Corte C, Grilli ST. Numerical modeling of extreme wave slamming on cylindrical offshore support structures. *Proceedings of the 16th Offshore and Polar Engineering Conference*, San Francisco, CA, U.S.A., vol. 3, 2006; 394–401.
14. Gilbert RW, Zedler EA, Grilli ST, Street RL. Progress on nonlinear-wave-forced sediment transport simulation. *IEEE Journal of Oceanic Engineering* 2007; **32**(1):236–248.
15. Zang Y. On the development of tools for the simulation of geophysical flows. *Ph.D. Thesis*, Stanford University, 1993.
16. Zang Y, Street RL. Numerical simulation of coastal upwelling and interfacial instability of a rotating and stratified fluid. *Journal of Fluid Mechanics* 1995; **305**:47–75.
17. Fringer OB, Street RL. The dynamics of breaking progressive interfacial waves. *Journal of Fluid Mechanics* 2003; **494**:319–353.
18. Zedler EA, Street RL. Large-eddy simulation of sediment transport: currents over ripples. *Journal of Hydraulic Engineering* 2001; **127**(6):444–452.
19. Zedler EA, Street RL. Large-eddy simulation of sediment transport: currents over ripples. *Journal of Hydraulic Engineering* 2006; **132**(2):180–193.
20. Kim K, Sirviente AI, Beck RF. The complementary RANS equations for the simulation of viscous flows. *International Journal for Numerical Methods in Fluids* 2005; **48**:199–229.
21. Alessandrini B. Thèse d'habilitation en vue de diriger les recherches. *Ph.D. Thesis*, Ecole Centrale de Nantes, 2007.

DOI: 10.1002/fld

22. Cui A, Street RL. Large-eddy simulation of turbulent rotating convective flow development. *Journal of Fluid Mechanics* 2001; **447**:53–84.
23. Grilli ST, Harris JC, Greene N. Modeling of wave-induced sediment transport around obstacles. *Proceedings of the 31st Coastal Engineering Conference*. World Scientific Publishing Company: Hamburg, Germany, 2009; 1638–1650.
24. Chou YJ, Fringer OB. Modeling dilute sediment suspension using large-eddy simulation with a dynamic mixed model. *Physics of Fluids* 2008; **20**:115103.1–115103.13.
25. Chou YJ, Fringer OB. Consistent discretization for simulations of flows with moving generalized curvilinear coordinates. *International Journal for Numerical Methods in Fluids* 2009; **62**:802–826.
26. Salon S, Armenio V, Crise A. A numerical investigation of the Stokes boundary layer in the turbulent regime. *Journal of Fluid Mechanics* 2007; **570**:253–296.
27. Radhakrishnan S, Piomelli U. Large-eddy simulation of oscillating boundary layers: model comparison and validation. *Journal of Geophysical Research* 2008; **113**(C02022):14.
28. Grilli ST, Guyenne P, Dias F. A fully nonlinear model for three-dimensional overturning waves over arbitrary bottom. *International Journal for Numerical Methods in Fluids* 2001; **35**(7):829–867.
29. Dean RG, Dalrymple RA. *Water Wave Mechanics for Engineers and Scientists*, Advanced Series on Ocean Engineering, vol. 2. World Scientific Publishing Company: Singapore, 1991.
30. Kajiura K. A model for the bottom boundary layer in water waves. *Journal of Fluid Mechanics* 1968; **182**:369–409.
31. Grant WD, Madsen OS. Combined wave and current interaction with a rough bottom. *Journal of Geophysical Research* 1979; **84**(C4):1797–1808.
32. Trowbridge JH, Madsen OS. Turbulent wave boundary layers: 1. Model formulation and first order solution. *Journal of Geophysical Research* 1984; **89**(C5):7989–7997.
33. Davies AG. A model of oscillatory rough turbulent boundary flow. *Estuarine*, *Coastal and Shelf Science* 1986; **23**(3):353–374.
34. Blondeaux P. Turbulent boundary layer at the bottom of gravity waves. *Journal of Hydraulic Research* 1987; **25**:447–464.
35. Aydin I, Shuto N. An application of the $k-\varepsilon$ model to oscillatory boundary layers. *Coastal Engineering in Japan* 1988; **30**(2):11–24.
36. Justesen P. Prediction of turbulent oscillatory flow over rough beds. *Coastal Engineering* 1988; **12**:257–284.
37. Justesen P. A note on turbulence calculations in the wave boundary layer. *Journal of Hydraulic Research* 1991; **29**:699–711.
38. Thais L, Chapalain G, Smaoui H. Reynolds number variation in oscillatory boundary layers. Part I. Purely oscillatory motion. *Coastal Engineering* 1999; **36**:111–146.
39. Mellor G. Oscillatory bottom boundary layers. *Journal of Physical Oceanography* 2002; **32**(11):3075–3088.
40. Tanaka SH, Sana A. Characteristics of turbulent boundary layers over a rough bed under saw-tooth waves and its application to sediment transport. *Coastal Engineering* 2008; **55**(12):1102–1112.
41. Kamphuis JW. Friction factor under oscillatory waves. *Journal of Waterways*, *Harbors Coastal Engineering Division* (ASCE) 1975; **101**:135–144.
42. Sleath JFA. Velocity measurements close to the bed in a wave tank. *Journal of Fluid Mechanics* 1970; **42**:111–123.
43. Jensen BL, Sumer BM, Fredsoe J. Turbulent oscillatory boundary layers at high Reynolds numbers. *Journal of Fluid Mechanics* 1989; **206**:265–297.
44. Jonsson IG, Carlsen NA. Experimental and theoretical investigations in an oscillatory turbulent boundary layer. *Journal of Hydraulic Research* 1976; **14**(1):45–60.
45. Sleath JFA. Transition in turbulent oscillatory flow over rough beds. *Journal of Waterways*, *Harbors Coastal Engineering Division* (ASCE) 1988; **114**:18–33.
46. Hino M, Kashiwanayagi M, Nakayami A, Hara T. Experiments on the turbulence statistics and the structure of a reciprocating oscillatory flow. *Journal of Fluid Mechanics* 1983; **131**:363–400.
47. Pope SB. *Turbulent Flows*. Cambridge University Press: Cambridge, 2000.
48. Sleath JFA. Turbulent oscillatory flow over rough beds. *Journal of Fluid Mechanics* 1987; **182**:369–409.
49. Longuet-Higgins MS. Mass transport in water waves. *Philosophical Transactions of the Royal Society of London A* 1953; **245**:535–581.
50. Longuet-Higgins MS. The mechanics of the boundary layer near the bottom in a progressive wave. *Proceedings of the Sixth International Conference on Coastal Engineering*, Gainesville, FL, U.S.A., 1958; 184–193.
51. Johns B. Residual flow and boundary shear stress in the turbulent bottom layer beneath waves. *Journal of Physical Oceanography* 1977; **7**:733–738.
52. Jacobs SJ. Mass transport in a turbulent boundary layer under a progressive water wave. *Journal of Fluid Mechanics* 1984; **146**:303–312.
53. Hsu TW, Ou SH. On the mass transport of water waves in a turbulent boundary layer. *Ocean Engineering* 1994; **21**(2):195–206.
54. Chowdhury AC, Sato M, Ueno A. Numerical model of the turbulent wave boundary layer induced by finite amplitude water waves. *Applied Ocean Research* 1997; **19**:201–209.
55. Deigaard R, Jacobsen JB, Fredsøe J. Net sediment transport under wave groups and bound long waves. *Journal of Geophysical Research* 1999; **104**(C6):13559–13575.
56. Davies AG, Villaret C. Eulerian drift induced by progressive waves above rippled and very rough beds. *Journal of Geophysical Research* 1999; **104**(C1):1465–1488.

DOI: 10.1002/fld

57. Myrhaug D, Holmedal LE. Bottom friction caused by boundary layer streaming beneath random waves for laminar and smooth turbulent flow. *Ocean Engineering* 2005; **32**(2):195–222.
58. Scandura P. Steady streaming in a turbulent oscillating boundary layer. *Journal of Fluid Mechanics* 2007; **571**:265–280.
59. Holmedal LE, Myrhaug D. Wave-induced steady streaming, mass transport and net sediment transport in rough turbulent ocean bottom boundary layers. *Continental Shelf Research* 2009; **29**:911–926.
60. Mei CC. *The Applied Dynamics of Ocean Surface Waves* (2nd edn), Advanced Series on Ocean Engineering. World Scientific Publishing Company: Singapore, 1989.
61. Longuet-Higgins MS, Cokelet ED. The deformation of steep surface waves on water. I. A numerical method of computation. *Proceedings of the Royal Society of London. Series A, Mathematical and Physical Sciences* 1976; **350**(1660):1–26.
62. Russell RCH, Osorio JDC. An experimental investigation of drift profiles in a closed channel. *Proceedings of the 6th Coastal Engineering Conference*, Gainesville, FL, U.S.A., 1958; 171–193.
63. Collins JI. Inception of turbulence at the bed under periodic gravity waves. *Journal of Geophysical Research* 1963; **68**(21):6007–6014.
64. Johns B. On the mass transport induced by oscillatory flow in a turbulent boundary layer. *Journal of Fluid Mechanics* 1970; **43**:177–185.
65. Brebner A, Askew JA, Law SW. The effect of roughness on the mass-transport of progressive gravity waves. *Proceedings of the 10th Coastal Engineering Conference*, Tokyo, Japan, 1966; 175–184.
66. Bijker EW, Kalkwijk JPT, Pieters T. Mass transport in gravity waves on a sloping bottom. *Proceedings of the 14th Coastal Engineering Conference*, Copenhagen, Denmark, 1974; 24–28.
67. van Doorn T. Experimental investigation of near-bottom velocities in water waves without and with a current. *Technical Report*, Delft Hydraulics Laboratory, 1981.
68. Ribberink JS, Al-Salem AA. Sheet flow and suspension of sand in oscillatory boundary layers. *Coastal Engineering* 1995; **25**:205–255.
69. Marin F. Eddy viscosity and Eulerian drift over rippled beds in waves. *Coastal Engineering* 2004; **50**(3):139–159.
70. Leonard BP. A stable and accurate convective modeling procedure based on quadratic upstream interpolation. *Computer Methods in Applied Mechanics and Engineering* 1979; **19**:59–98.
71. Moeng CH. A large-eddy simulation model for the study of planetary boundary-layer turbulence. *Journal of Atmospheric Science* 1984; **46**:2311–2330.
72. Cabot W, Moin P. Approximate wall boundary conditions in the large-eddy simulation of high Reynolds number flows. *Flow, Turbulence, and Combustion* 1999; **63**:269–271.
73. Piomelli U, Balaras E. Wall-layer models for large-eddy simulation. *Annual Review of Fluid Mechanics* 2002; **34**:349–374.
74. Nakayama A, Noda H, Maeda K. Similarity of instantaneous and filtered velocity fields in the near wall region of zero-pressure gradient boundary layer. *Fluid Dynamics Research* 2004; **35**:299–321.
75. Smagorinsky J. General circulation experiments with the primitive equations, I. The basic experiment. *Monthly Weather Review* 1963; **91**:99–164.
76. Lilly DK. Representation of small scale turbulence in numerical simulation experiments. *IBM Scientific Computing Symposium on Environmental Sciences*, Yorktown Heights, New York, U.S.A., 1967; 195–210.
77. Germano M, Piomelli U, Moin P, Cabot WH. A dynamic subgrid-scale eddy viscosity model. *Physics of Fluids A* 1991; **3**(7):1760–1765.
78. Lilly DK. A proposed modification of the Germano subgrid-scale closure method. *Physics of Fluids A* 1992; **4**(3):633–635.
79. Germano M. Turbulence: the filtering approach. *Journal of Fluid Mechanics* 1992; **238**:325–336.
80. Lund TS. On the use of discrete filters for large eddy simulation. *Technical Report*, Annual Research Briefs, Center for Turbulence Research, 1997.
81. Germano M. A proposal for a redefinition of the turbulent stresses in the filtered Navier–Stokes equations. *Physics of Fluids* 1986; **29**:2323–2324.
82. Vasilyev OV, Lund TS, Moin P. A general class of commutative filters for LES in complex geometries. *Journal of Computational Physics* 1998; **146**:82–104.
83. Chow FK, Street RL. Explicit filtering and reconstruction turbulence modeling for large-eddy simulation of field-scale flows. *Advances in Hydro-science and Engineering* 2004; **6**:1–12.
84. Chow FK, Street RL, Xue M, Ferziger JH. Explicit filtering and reconstruction turbulence modeling for large-eddy simulation of neutral boundary layer flow. *Journal of the Atmospheric Sciences* 2005; **62**:2058–2077.
85. Piomelli U, Balaras E, Pasinato H, Squires KD, Spalart PR. The inner–outer layer interface in large-eddy simulations with wall-layer models. *International Journal of Heat and Fluid Flow* 2003; **24**:538–550.
86. Stokes GG. On the effect of the internal friction of fluids on the motion of pendulums. *Cambridge Philosophical Transactions* 1851; **9**:8–106.
87. Nielsen P. *Coastal Bottom Boundary Layers and Sediment Transport*, Advanced Series on Ocean Engineering, vol. 4. World Scientific Publishing Company: Singapore, 1992.
88. Costamagna P, Vittori G, Blondeaux P. Coherent structures in oscillatory boundary layers. *Journal of Fluid Mechanics* 2003; **474**:1–33.
89. Scandura P. Measurements of wave-induced steady currents outside the surf zone. *HYDRALAB III Joint User Meeting*, Hannover, Germany, 2010.

DOI: 10.1002/fld